TEST FOR SUBSTRUCTURE IN THE LENSING GALAXY OF RADIO-QUIET QUASAR LENSES BY RADIO IMAGING

A thesis submitted to the University of Manchester
for the degree of Master of Science
in the Faculty of Engineering and Physical Sciences

July 2014

By
Carl Roberts
School of Physics and Astronomy

Contents

List of Tables

List of Figures

Abstract

This paper examines the viability of studying substructure in lens systems by radio imaging of the radio-quiet lens systems HE0435-1223 and RXJ0911+0551. The observations are carried out by the JVLA, the data reduction is done in AIPS and the modelling is performed by the Igloo modelling software. In HE0435-1223, one of the images is found to be much fainter in the optical than in the radio, which may be due to either microlensing or dust extinction. This means that the flux ratio anomaly in Fadely, Keeton [Fadely and Keeton, 2012b] is not caused by substructure and the radio fluxes can be well fitted by a smooth SIE model. Therefore, there is no evidence for a subhalo as claimed in [Fadely and Keeton, 2012b]. In RXJ0911+0551, two of the images are affected by dust extinction. The cusp relation violation is still present, for the *JMFIT* fluxes $R_{cusp} = 0.092 \pm 0.018$ (where *JMFIT* is a program in AIPS which fits Gaussian models to an image) and for the Difmap fluxes $R_{cusp} = 0.143$. Both are significantly lower than the near-infrared [Keeton et al., 2003] $R_{cusp} = 0.23 \pm 0.06$. This indicates that substructure is possibly in the system, but the revised cusp violation is not as strong as previously thought.

University of Manchester,
Carl Roberts
Master of Science
6 April 2014
Oxford Road,
Manchester,
M13 9PL.
Jodrell Bank Centre for Astrophysics,
Alan Turing Building,

Supervisor : Dr Neal Jackson
Advisor: Dr Myfanwy Lloyd

Declaration

No portion of the work referred to in this thesis has been submitted in support of an application for another degree or qualification of this or any other university or other institution of learning.

Carl Roberts
Jodrell Bank Centre for Astrophysics
Alan Turing Building
The University of Manchester
Oxford Road
Manchester
M13 9PL
U.K.

Copyright

Acknowledgements

I would like to thank my supervisor Dr Neal Jackson for his help and advice, my family for their constant support and encouragement and my friends David Boulderstone, Philippa Hartley and Nick Wrigley for their help editing this paper and in using AIPS.

Chapter 1

Introduction

1.1 The missing satellites problem

The formation and expansion of structure in the Universe is thought have happened by hierarchical accretion, where the clustering process is dominated by dark matter halos. Small, low mass halos form earliest then merge to form galaxies and then clusters. This is a well established cosmological model capable of reproducing accurately the large scale structure of the Universe. The hierarchical model can reproduce the formation of clusters of galaxies, for when a galaxy and its dark matter halo are accreted onto a cluster, the less tightly bound regions of the halo are stripped away by gravitational effects, but the centre of the halo containing the galaxy survives.

In theory, galaxies are formed by the same process as clusters except at a smaller scale. However, simulations of dark matter particles used to study the formation of galactic halos found that the number of subhalos within a galaxy follow a power law:

$$\frac{dN}{dM_{sub}} \propto M_{sub}^{-\alpha},$$

with $\alpha \approx 1.9$, so the Milky Way's halo should contain about 500 satellites within its virial radius [Moore et al., 1999, Klypin et al., 1999]. But when [Moore et al., 1999] was published, only 11 satellites of the Milky Way were known within the virial radius.

This excess of satellites is still seen in current simulations [Boylan-Kolchin et al., 2011] resolving particle masses of $M_{sub} \sim 10^3 M_\odot$, therefore it is not an artifact of poor resolution. This picture has recently been complicated by simulations which predict that there should be between 6 and 12 dark subhalos orbiting the Milky Way which are as massive as the luminous MW satellites but are not luminous [Boylan-Kolchin et al., 2011]. This is due to the subhalos being too dense to host bright dwarf spheroidal galaxies. This problem has been named the “too big to fail” problem.

CDM predicts far more low mass subhalos orbiting the Milky Way than have been observed. To resolve this, there are a variety of solutions which either destroy/prevent the subhalos from forming, or inhibit star formation, leaving a population of dark satellites. Some the solutions include warm [Menci et al., 2012] or self-interacting dark matter [Vogelsberger et al., 2012] preventing subhaloes from forming, tidal forces from the galactic disk ripping the haloes apart [D'Onghia et al., 2010] and the supernovae of the first generation of stars in the haloes expelling most of the gas, inhibiting later star formation [Dekel and Silk, 1986]. So one set of explanations for the ”missing satellites” will leave a population of dark satellites orbiting the Milky Way, whereas in the other case there is no such population. This naturally begs the question of how do we discover these hidden satellites that are too faint to observe directly.

One way they can be detected is by using gravitational lensing. Equally, if there are no lensing events due to dark satellites, then solutions that prevent subhalos from forming are favourable. Herein is a description of the techniques used to detect dark satellites of lens galaxies, beginning with a quick summary of lens theory and a brief discussion over uncertainties in the density profile of satellite galaxies.

1.1.1 Lens background

Light from a source can be deflected by the gravitational potential of a lensing galaxy between the observer and the source. From [Scheider et al., 2006], we see in a weak gravitational field, with no other masses along the line of sight, that:

$$\beta = \theta - \frac{D_{ls}}{D_s}\hat{\alpha}(D_l\theta) \equiv \theta - \alpha(\theta),$$

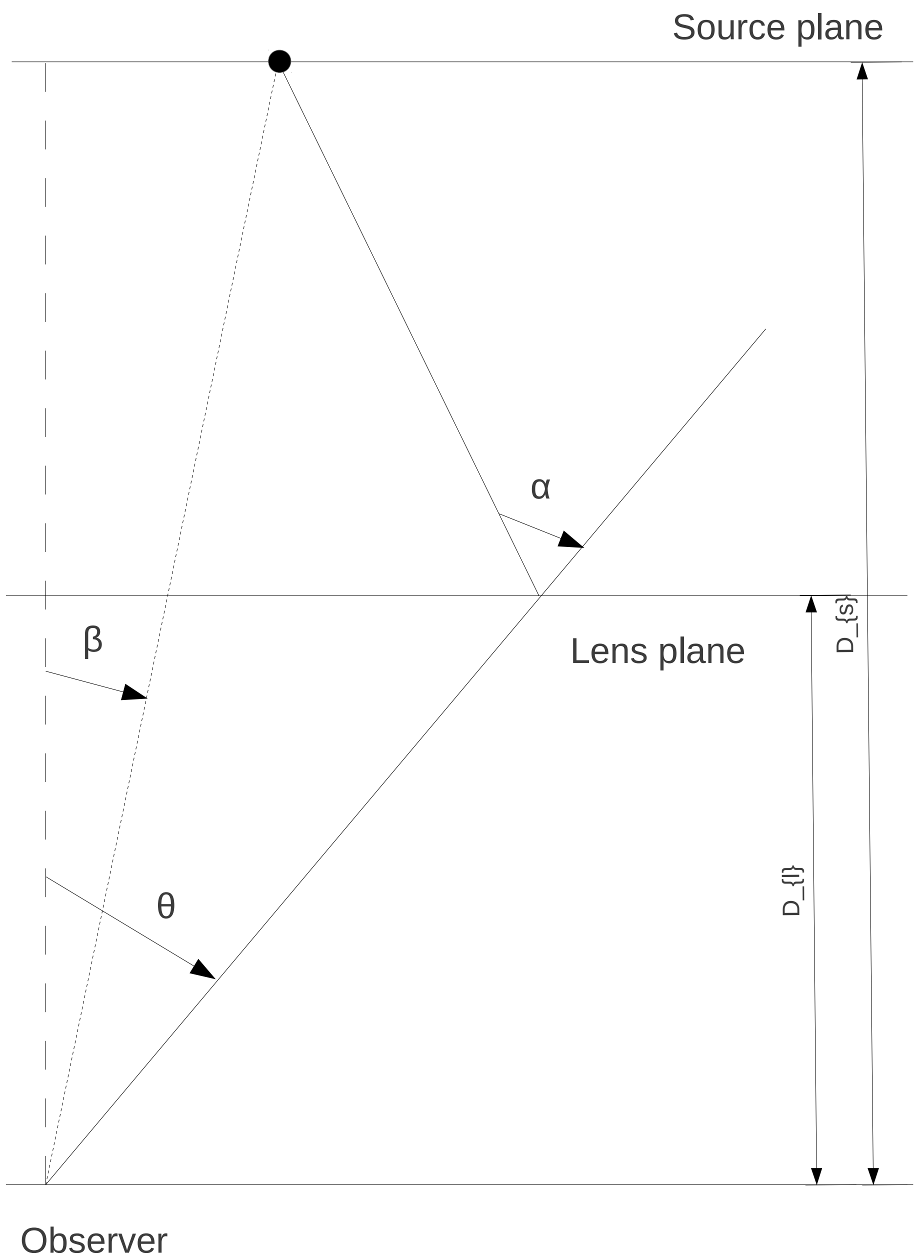

Figure 1.1: A diagram of a general gravitational lens system.

where β is the true position of the source, θ is the perceived position of the source, $\hat{\alpha}$ is the deflection angle, $\alpha(\theta)$ is the scaled deflection angle, D_l is the distance between observer and the lens plane, containing the lens galaxy, D_s is the distance between observer and source plane, containing the source, and $D_{ls} = D_s - D_l(1 + z_l)/(1 + z_s)$. This can be expressed in terms of surface mass density:

$$\alpha(\theta) = \frac{1}{\pi} \int_{\mathbb{R}^{\not{\leq}}} d^2\theta' \kappa(\theta') \frac{\theta - \theta'}{|\theta - \theta'|^2},$$

where the dimensionless surface mass density, $\kappa(\theta)$, is:

$$\kappa(\theta) := \frac{\sum(D_l\theta)}{\sum_{cr}},$$

with the critical density, $\sum_{cr}$, being:

$$\Sigma_{cr} = \frac{c^2}{4\pi G} \frac{D_s}{D_l D_{ls}}.$$

The distortion of images is described by the Jacobian:

$$A(\theta) = \frac{\delta\beta}{\delta\theta},$$

which allows us to define the magnification, μ, by:

$$\mu = \frac{1}{det(A)}.$$

So if the Jacobian is zero, then the magnification is infinite. We define the critical lines to be the curves in the lens plane where the magnification tends to infinity. By mapping the critical curves onto the source plane, a set of caustic curves is generated. The caustic curves have two parts, the smooth lines, which are called folds, and the points were two folds meet, which are called cusps.

1.1.2 Density distribution of satellite galaxies

When creating a lens model, it is necessary to know the density profiles of the galaxies and the subhalos. The standard density profile in cold dark matter models is the NFW profile [Navarro et al., 1997]:

$$\rho_{NFW}(r) = \frac{\rho_i}{(r/r_S)(1 + r/r_S)^2},$$

where r_S is the characteristic scale radius of the halo and ρ_i is connected to the density of the Universe at the moment of collapse. This profile is typically used for the dark subhalos, since they have negligible bayronic mass. However, some argue that the NFW model does not give the best fit for subhalos, but the Einasto profile does [Vera-Ciro et al., 2013]. For modelling the lensing galaxy, baryons are far more important and are modelled by the Hernquist profile. In the region where strong lensing occurs, the sum of the NFW and Hernquist profiles can be approximated by a singular isothermal sphere (or SIS) [Zackrisson and Riehm, 2010], with a density profile of:

$$\rho_{SIS}(r) = \frac{\sigma^2}{2\pi G r^2},$$

where σ is the velocity dispersion along the line of sight.

1.2 Current observational situation

Currently, there are three different approaches to determining the existence of dark satellites: using radio lenses, structure mapping using optical lenses and, finally, submillimetre lenses. The main purpose of this paper is to demonstrate a fourth prong of attack, wherein we observe radio-quiet quasar lenses in the radio.

1.2.1 Radio lenses

Lensing theory tells us that an elliptical lens produces two caustics, one contained within the other. If the source is near the fold of the outer caustic curve, then an observer will see two images of the source, which will be produced near the critical line in the lens plane. The magnifications of these two images should be the same but with different parity; the flux ratio should be [Zackrisson and Riehm, 2010]:

$$R_{fold} = \frac{|A| - |B|}{|A| + |B|} \rightarrow 0,$$

tending to zero as separation between the images tends to zero ($A\&B$ are the magnifications of the two images). If the source is near a cusp, then three images of the source are produced close to each other near the critical line in the lens plane, with the flux ratio [Zackrisson and Riehm, 2010]:

$$R_{cusp} = \frac{|A| - |B| + |C|}{|A| + |B| + |C|} \rightarrow 0,$$

which is asymptotically small as separation decreases ($A\&B\&C$ are the magnifications of the three images).

However, these relations do not hold for the majority of observed lens systems. This was thought to be because of substructure in the lensing galaxy [Mao and Schneider, 1998]. By adding substructure to lens models to correct flux ratios, it was found [Dalal and Kochanek, 2002] that substructure comprised between 0.6% and 7% of the mass of the lens galaxy for satellites in the range of $10^{10} - 10^{13}$ solar masses. This was far more substructure than had been observed around the Milky Way, so sources of systematic error were sought, in order to accurately determine the luminosity function.

One source of error, scattering and extinction due to the ISM, was considered unlikely because the flux ratio anomalies are dependent on image parity and magnification, whereas the ISM would affect the images equally, regardless of the parity and magnification [Kochanek and Dalal, 2004]. Additionally, the flux anomalies were independent of wavelength, but scattering and extinction by ISM depend heavily on wavelength. To remove the possibility of effects from the ISM, measurements were made of PG1115+080 and B1422+23 [Chiba et al., 2005] in the mid-infrared, which is known to be unaffected by the ISM, proving that the mid-infrared flux anomalies are in close agreement with the radio fluxes.

Microlensing by stars has been known to affect flux ratios of images viewed in the visible spectrum. This is because the light emitted from the quasar comes predominately from a compact region, comparable in size to the Einstein radius of the stars within the lensing galaxy. However, radio emission comes from a much larger region, so the Einstein radius of a star within the lensing galaxy is tiny. So the net effect of positive and negative magnification by many stars is nil, since they cancel each other.

Another issue in finding substructure is that flux ratios are highly sensitive to the shape of the lens galaxy, particularly the ellipticity [Metcalf and Amara, 2012a]. However, adding higher order multipoles to lens models made little improvement and could not reproduce the parity dependence of the flux anomalies [Kochanek and Dalal, 2004], so are unlikely to be a major factor.

Finally, a major systematic error is the mass-sheet degeneracy. Using the Millennium II simulations [Xu et al., 2012], it was discovered that objects along the line of sight, particularly halos behind the lens, could be as or even more important than lens substructure in causing flux anomalies, and that combining these two effects could remove the discrepancy between models and observations. Modelling to correct flux anomalies in HE0435-1223 [Fadely and Keeton, 2012a] has found that the mass fraction of subhalos near the Einstein radius in this lens system is > 0.00077, which is compatible with CDM predictions.

An additional test for dark satellites is that if we have a lensed quasar then if a dark matter subhalo intersects the line of sight to the quasar, then the image may be distorted or split, with these effects occurring on the $1 \sim 30$ milliarcsecond scale [Yonehara et al., 2003]. This was advanced by [Inoue and Chiba, 2005], who calculated that using ALMA subhalos of mass $\sim 10^{12}$ solar masses that are a few kpc away from the centre of the lens galaxy could be detected. In addition, it was demonstrated [Inoue and Chiba, 2005] that if measured in the submillimetre range, measuring the astrometric shifts for multiple images could break the degeneracy between substructure mass and the distance along the line of sight to the lens galaxy.

Although this method does not suffer from ISM contamination or microlensing by stars, there is the possibility that globular clusters can create distortions and splitting that looks like the work of dark subhalos. This theory was proposed [Bukhmastova, 2007] as an explanation for quasars that are close in redshift as well as separation on the sky, which are termed close pairs. It was suggested [Bukhmastova, 2007] that the light from the core of a distant galaxy was split and magnified by the globular clusters of the nearby galaxy. Another issue is that the predictions for the scale the effects occur used the singular isothermal sphere model, which greatly exaggerates the scale [Zackrisson et al., 2008] and using the most favoured, recent density profiles for the subhalos may make the separation too small to resolve for any current telescope or any currently being built.

When the images of a lensed quasar are altered by substructure near to the images in the lens plane, their time delays are perturbed by the subhalos. These time delays are due to a combination of differences in path lengths and Shapiro time delays (i.e. time delays due to deep gravitational fields). So the time delays can be used to examine the substructure around the lensing galaxy. This method requires quasars, since some are known to vary in luminosity on timescales of hours or more. This was investigated [Keeton and Moustakas, 2009] and it was shown that time delay ratios do not suffer from the radial profile degeneracy, dust extinction and stellar microlensing. Another advantage is that it examines a different part of the mass-function, time delay perturbations depend on m^2 [Keeton and Moustakas, 2009], whereas astrometric perturbations depends on $m^{3/2}$ and anomalous flux ratios depend on m, where m is the mass of the perturbing subhalo. Using this method, two lens systems B122+231 and XJ0911+0551 showed [Congdon et al., 2010] evidence of substructure, but big uncertainties in the observed time delays prevented a strong conclusion.

If the substructure of the lensing galaxy causes image splitting that cannot be resolved, then the brief time lags between the light from the two images result in an echo effect in the light curve of objects with short term variability. Suitable objects include gamma-ray bursts and X-ray quasars. To measure CDM subhalos, it is better to use X-ray quasars [Yonehara et al., 2003], whose time delay should be $1 \sim 10^3$ seconds and are more likely to be lensed by a galaxy, so the likelihood of any time delay perturbations being due to dark subhalos is increased.

1.2.2 Structure mapping

In systems with a lensing galaxy, halo substructure may alter the deflection caused by the lens galaxy and so the positions of the images will be shifted, which is termed astrometric perturbations. This method is relatively unaffected by contamination by the ISM but is only sensitive to intermediate and high mass subhalos, so it investigates a higher mass region than measuring flux ratio anomalies. However, simulations showed [Metcalf and Madau, 2001] that to alter the image position by a few tens of a milliarcsecond would require subhalos of the order $\gtrsim 10^{12}$ solar masses in precise alignment with the source, but such an event is very unlikely to occur. An additional difficulty is that perturbations from substructure are partly degenerate with the smooth lens galaxy model [Chen et al., 2007], where image perturbations for a lens galaxy with little or no substructure is $\geq$ 10mas, which is an order of magnitude larger than the expected astrometric shift from substructure.

Another technique has been developed which is mass reconstruction via an adaptive-grid method [Vegetti and Koopmans, 2009], which uses Bayesian analysis of Einstein rings. This is independent of the properties of dark matter, the shape, density and dynamics of the host galaxy and its satellites. Simulations with mock data showed [Vegetti and Koopmans, 2009] that this method could detect subhalos down to a mass of 3×10^{12} solar masses. Further testing proved that this could detect the presence of a known luminous satellite in J120602.09+514229.5 [Vegetti et al., 2010] and provide a mass estimate for it, as well as reproducing the host galaxy's density profile. Confident in this technique, it was applied to JVAS B1938+666 and SDSS J0946+1006 [Vegetti et al., 2012] and constrained the average amount of mass in substructures to be $f = 3.3^{+3.6}_{-1.8}\%$ and the slope of the mass-function to be $\alpha = 1.1^{+0.6}_{-0.4}$ at a 68% confidence level, which is in agreement with cold dark matter models.

1.2.3 Submillimetre lenses

Recently with the advent of ALMA, there is a new way to look for substructure in lens systems, by making submillimetre observations of dusty, star-forming galaxies (DSFGs) lensed by foreground galaxies. These DSFGs are typically found at high redshift, $2 < z < 5$. As their name implies, DSFGs contain large amounts of dust, but also contain massive molecular clouds. This gas is excited by the intense radiation from the active star-forming regions, hence these galaxies are typically observed to have strong molecular lines. Frequently seen lines include CO, H_2O and HCN. Therefore, submillimetre radiation from DSFGs is currently thought to be dominated by many regions with high star formation rates distributed throughout the galaxy. These compact regions are much smaller than the galaxy and are sensitive to lensing perturbations by substructure much smaller than the size of the substructure that the galaxy is sensitive to, because a uniform source is uneffected by lensing perturbations form structures small compared to the source size.

However, in practice what is seen are many overlapping, merged sources, which look like an extended source and thus are less sensitive towards substructure lensing. But there is a method to decompose the received emission into its components. Spectroscopic observations of DSFGs show that they have large velocity gradients, either from quickly rotating disks or from recent merges. Provided that the difference in the velocity of the star forming clumps along the line of sight is greater than the velocity dispersion within the clumps, then by observing at different frequencies, distinct clumps can be distinguished. So the emission from a thin frequency band will come from a small region of the DSFG.

Lensed DSFGs are useful for examining substructure, particularly because there are a large number of them already known; roughly 100 have been found in large field millimetre surveys. Another useful feature is that the dust in the DSFGs absorbs almost all the UV and optical flux and re-emits it in the infrared, so they are almost invisible in the optical. In the case that substructure is found via gravitational lensing, then deep optical imaging will be able to place better constraints on the mass to light ratios of the subhalos, because the host galaxy is fainter than it ordinarily would be. Additionally, the large range of redshifts of DSFGs mean that is a wide range of potential lens redshifts, thereby allowing restrictions to be placed on any evolution in the substructure population with redshift. An additional advantage of this method is that it allows the examination of the ISM of DSFGs at higher redshifts than previously possible.

Finally, as was discussed in [Hezaveh et al., 2013a], observing different molecular lines changes what subhalo mass to which the measurements are sensitive. This is because each molecular line has its own critical density, so these lines trace regions with different densities and sizes of gas clouds, and smaller sources within the DSFG are more sensitive to the effects of lensing by lower mass subhalos in the lensing galaxy. Furthermore, results from [Hezaveh et al., 2013a] predict that while there is a higher probability of detecting subhalos in high magnification fold and cusp lenses, low magnification and double lenses also have some sensitivity to substructure, unlike quasar lenses.

Recently, ALMA has performed follow up observations of four suspected lensed DSFGs that were found by the SPT [Hezaveh et al., 2013b], and were not only able to confirm that these are lens systems, but also were able to obtain the redshifts of the galaxies and fit a lens model to the data. Similarly, [Wardlow et al., 2013] nine strong lensed DSFGs were found using Herschel-SPIRE photometry from the HerMES survey.

1.3 Radio-quiet quasar lenses

The main difficulty in studying flux anomalies in radio loud quasar lens systems is that the results suffer from bias caused by small sample sizes. This is because there are only a dozen quadruply lensed, radio-loud quasars currently known. However, the improved sensitivity of JVLA has provided a means to improve on the sample size, and hence, improve the constraints on substructure orbiting lensing galaxies. This is the study of radio-quiet lens systems, which have already been found in the optical or infra-red wavelengths.

This method has all the advantages of observing radio-loud quasars. Additionally, these lens and some radio-loud lenses have previously been observed in the optical or infra-red wavelengths, so comparing the results at different frequencies can reveal differences in flux density and variability between different wavelengths. In particular, because radio data reveals the intrinsic flux ratios of the images without distortion from microlensing, the effect of microlensing on the optical flux ratios of the lens system can be found. This was demonstrated in [Jackson, 2011] where the lens system J1004+4112 was observed in radio by the EVLA and then followed up three months later by optical observations. It was found that the radio fluxes were consistent with models, but also that image C in J1004+4112 was considerably brighter in the optical observations than in the radio. This indicated that either image C was going through a high magnitude microlensing event or that it was undergoing a rapid and intense change in the intrinsic variability of the brightness of the quasar.

Another feature of this method is that it can be used to obtain highly magnified images of radio-quiet quasars. This will enable a closer examination of the mechanism that produces radio emission in these inactive quasars. These quasars are strongly accreting but they lack the large scale jets of radio-loud quasars, which serve to transport energy and angular momentum away from the nuclei. Indeed, the core luminosities of radio-quiet quasars can be as high as the radio-loud quasars. Currently, it is thought [Blundell and Kuncic, 2007] that the radio core emission has a large contribution from optically thin bremsstahlung radiation from a slow, dense disk wind. This disk wind plays the role that the jets perform, by taking away angular momentum from the accretion disk. In fact, it is theorised [Blundell, 2008] that over the lifetime of a quasar it is predominantly radio-quiet, but occasionally it will flare up and produce radio jets, thereby becoming radio-loud.

Chapter 2

Data Analysis

In this chapter, I shall explain how the JVLA was used to observe the radio-quiet lens systems HE0435-1223 and RXJ0911+0551. Firstly, there will be a brief introduction to interferometry [Thompson et al., 2001]. Then, I will describe how the observations were performed. Finally, I shall detail what was done to the data in order to produce the maps of the two lens systems.

2.1 Interferometry

2.1.1 Fundamental theory

One way to understand interferometry is to examine a basic two-element interferometer using simplifying assumptions, then look at how we correct for the fact that these assumptions rarely apply in practice. The following diagram shows a representation of a two-element interferometer, where the antennae are pointing along vector s at a radio source, which we assume is distant enough that the received waves are planar. One antenna detects the wavefront from the source earlier than the other, the time difference between the antennae is called the geometric delay, τ and is given by:

$$\tau = b.s/c,$$

where c is the speed of light and b is the baseline vector, which is the vector pointing from one antenna to the other.

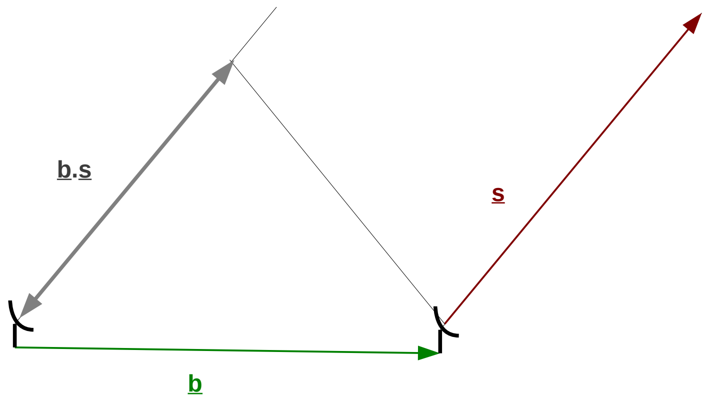

Figure 2.1: A basic two-element interferometer.

Therefore, the waves received by the antennae are out of phase with each other by τ seconds. The voltage produced by the antennae are multiplied together by a correlator, which allows these waves to constructively or destructively interfere in a similar manner to the Young's slit experiment. If in the interferometer there is a variable delay-line, then the delay can be varied until the waves maximally constructively interfere. The phase difference where this occurs is related to the position of the source on the sky and the intensity of the source is proportional to the square of the voltage output of the antenna.

The intensity of the sky, $I(x, y)$, is known as the sky brightness distribution. However, the interferometer observes the interference between the antennae. The measurements of interference made by an array of delays is known as a set of visibilities. Ideally, the sky brightness and visibilities are Fourier transforms of one another:

$$V(u, v) = \iint I(x, y) exp[-2\pi i(ux + vy)]dxdy,$$

where $V(u, v)$ is the visibility in a 2D-plane, where u and v are the coordinates with units of wavelengths. The 'uv-plane' is referred to as the Fourier plane. Hence, the sky brightness can be retrieved by performing the inverse Fourier transform on the observed visibilities. However, this is the ideal case, in reality there are many complications which need to be corrected.

2.1.2 Complications

For an interferometer, the delay between the reference telescope and any other telescope is not just the geometric delay. One additional source of delay comes from the electronics in the telescope and the writing to the correlator. Another is water vapour in the atmosphere and charged particles in the ionosphere. Because each telescope looks through a different part of the atmosphere, the atmospheric conditions for each antenna are different, therefore, the delay caused by atmospheric effects differs for each antenna. Moreover, atmospheric conditions alter rapidly so the delays change, with timescales ranging from minutes to hours.

The solution is to observe a bright calibrator source whose intensity and, therefore, visibilities are already known. Then the true amplitude and phase are compared with the observed to obtain the errors for each antenna; this process is called fringe fitting. The complex gain G_{ij} for a baseline defined by antennae i and j with observed visibilities $\hat{V_{ij}}$ is described using the true visibilities V_{ij} by:

$$\hat{V_{ij}}(t) = V_{ij} G_{ij}(t),$$

and the gain correction for each antenna is:

$$G_{ij}(t) = g_i(t)\bar{g}_j(t)g_{ij}(t),$$

where g_i is the complex correction for antenna i and $g_{ij}(t)$ is the closure error, which for good solutions should be close to one. This system of linear equations is then solved to find the complex correction for every antenna. By frequently observing the calibrator, solutions for periods when the calibrator is observed can be interpolated, allowing complete solutions across the observing time.

Another difficulty presented during observations is systematic error in the gain of the antennae at different frequencies. Each frequency channel has its own error in amplitude and phase. To correct this requires a bandpass calibration, where a bright calibrator is observed, whose relationship between flux and frequency is known. Since the true flux is known for each frequency channel, the error can be found and corrected.

An assumption made in theory is that $V(u, v)$ is known for all values of u and v. In practice, only some of the uv-plane is observed because there are not enough telescopes to cover the entire plane. With the baselines available, more uv coverage is attained by exploiting the rotation of the Earth, because the projected vectors change relative to the source. The uv coverage of an observation is described by the sampling function $S(u, v)$, which equals one if visibilities have been observed at that (u, v), or zero otherwise.

Theoretically, the sky brightness distribution $I(x, y)$ is found by taking the inverse Fourier transform of the set of visibilities $V(u, v)$. However, the observed visibilities, $O(u, v)$, are related to the true visibilities by [Thompson et al., 2001]:

$$O(u, v) = V(u, v) \times S(u, v)$$

But $S(u, v)$ is known, so to find $I(x, y)$ requires Fourier transforming $O(u, v)$ to get:

$$O'(x, y) = I(x, y) * S'(x, y)$$

where $S'(x, y)$ is the dirty beam and $O'(x, y)$ is the dirty map. Then the dirty map is deconvolved with the dirty beam, but deconvolution requires some information about $I(x, y)$ and different methods of deconvolution assume different properties about $I(x, y)$. In AIPS, deconvolution is performed by an algorithm called CLEAN, created by Clark and Högborn [Hogbom].

The CLEAN method of deconvolution assumes that $I(x, y)$ is comprised of a small number of discrete sources upon a background of noise. This method works by finding the brightest point in the dirty map, then partly subtracting the dirty beam from the dirty map and recording the intensity and position of the point as a clean component. The remainder of the dirty map is called the residual map. This procedure is iterated on the residual map until no more significant subtractions are made. The cleaned image is then comprised of the residual map combined with the clean components.

Another matter to consider is that sources near to declination zero have worse resolution in the North-South axis. This is because each baseline traces an ellipse in the uv-plane as the Earth rotates. However, if the source is equatorial, then the North-South component of the baseline vector varies by a smaller amount. Therefore, the closer the source is to declination zero, the flatter the ellipse becomes, collapsing to a straight line along the u-axis at declination zero. The North-South resolution depends on the width of the ellipse along the v-axis. The solution to this is to have have as many baselines as possible with different North-South components, so the baselines densely cover the v-axis of the uv-plane as possible.

2.2 Observational Parameters

For this paper, two radio-quiet lens systems were observed: HE0435-1223 and RXJ0911+0551. These systems were observed using the JVLA in the C-band. The observation periods for HE0435-1223 were two blocks of 3 hours on 26 October and 9 November 2012; RXJ0911+0551 had two blocks of 3 hours on 31 October and 6 November and one block of 90 minutes on 24 November 2012. The details of the observations may be found in Tables 2.1 and 2.2.

Lens System	Right Ascension	Declination
HE0435-1223	4:38:14.90	-12:17:14.4
RXJ0911+0551	9:11:27.50	5:50:52.0

Table 2.1: The positions of the lens systems on the celestial sphere in J2000 coordinates.

	Time Observed	Centre Freq	IF	Channels	Channel Width	Integration Time
HE0435-1223	6 hours	4.552 GHz	16	64	2 MHz	5 seconds
RXJ0911+0551	7.5 hours	4.552 GHz	16	64	2 MHz	5 seconds

Table 2.2: Parameters under which the lens systems were observed, including the number of IF's and channels. The bandwidth was 2.048 GHz for both sets of observations. The observations were made in full stokes.

All the measurements took place while the VLA was in configuration A, which has a maximum baseline of 36.4km, implying a maximum resolution of 0.37 arcseconds at C-band. A higher resolution may have been obtained by observing at a higher frequency, but the spectrum of a radio-quiet quasar is steep, so the source would be less intense. The observations required a good signal-to-noise ratio whilst still having a high enough angular resolution to resolve individual components of the lens systems, therefore the lenses were observed in the C-band.

To calibrate the data, each observing period also looked at a flux and a phase calibrator. For both HE0435-1223 and RXJ0911+0551 the flux calibrator was 3C138, because it is a bright, discrete source whose flux is known and has been modelled. The phase calibrator for HE0435-1223 was J0435-18441 and for RXJ0911+0551 it was J0914+02451. These were selected because they are also bright, compact sources that are close to the targets, so their phase solutions can be transferred to the objectives without much additional change in delay.

2.3 Calibrating the data and imaging

The task of editing, calibrating and imaging the data was performed using the AIPS program. A script was followed which is presented in the Appendix. Below is a brief description of the process, illustrated with examples of the process as performed on the October HE0435-1223 dataset.

The fits files were loaded into AIPS using the *FITLD* command, then bad data was identified, using *POSSM, LISTR* and *SPFLG* among other commands, and flagged (using *UVFLG*). *POSSM* plots amplitude and phase against IF and it was performed over the time period when the calibrator 3C138 was observed to identify channels where the amplitude or phase varies wildly or is zero. *LISTR* with the adverb *optype 'matx'* prints matrices containing the total flux received for each baseline over time periods shorter than ten minutes. This reveals any telescopes in the array which were malfunctioning or pointing in the wrong direction, in the example dataset antenna 17 between 8:21:43 and 8:30:53 was flagged for this reason. *SPFLG* plots an image for each baseline with channel on the x-axis and time on the y-axis and the brightness of the pixel is the flux received in that channel and time. Areas of anomalous brightness are removed as they are time and channels which were noisy. *SPFLG* comprised most of the edits, requiring an examination of a plot for each baseline.

After data editing, *CALRD* loaded an image of the calibrator source 3C138 from AIPS, which required fringe fitting the data using the function *FRING*. After fringe fitting, and each after subsequent calibration, the solutions were checked with *SNPLT* then applied to the dataset with *CLCAL*. Next, a bandpass calibration was performed by *BPASS*, using the model of 3C138 loaded previously. The effectiveness of these calibration can be seen for fringe fitting in the difference between Figures 2.1-2.2 and Figures 2.3-2.4, and for bandpass calibration between Figures 2.5-2.6 and Figures 2.7-2.8.

The 64 channels in each IF were averaged together into one channel, via *AVSPC*.

This speeds up the subsequent calibration and imaging but decreases the field-of-view by bandwidth smearing which is governed by $FOV = \theta \times f/\Delta f$, where θ is the resolution and Δf is the bandwidth. Inputting 0.37" and 128 MHz as the resolution and bandwidth give $FOV = 13.2''$ which is enough field-of-view since the lens systems are only a couple of arcseconds across. Then the flux density of the calibrator 3C138 was determined using *SETJY* and the flux calibration was applied to the target source via *GETJY*. *CALIB* creates a phase solution that corrects for phase changes over time by calculating the phase shifts on the phase calibrator over time and then extrapolating them and applying it to the target source data.

A separate uv-data file was made containing only the lens system using the *SPLIT* command and combined the data from each observation period together using *DBCON*. Finally the data was imaged using *IMAGR* with natural weighting, the cell size was 0.02" and the initial image size was 1024 pixels to remove any anomalous sources, but the final images below in Figures 2.9 and 2.10 are 512 pixels in size.

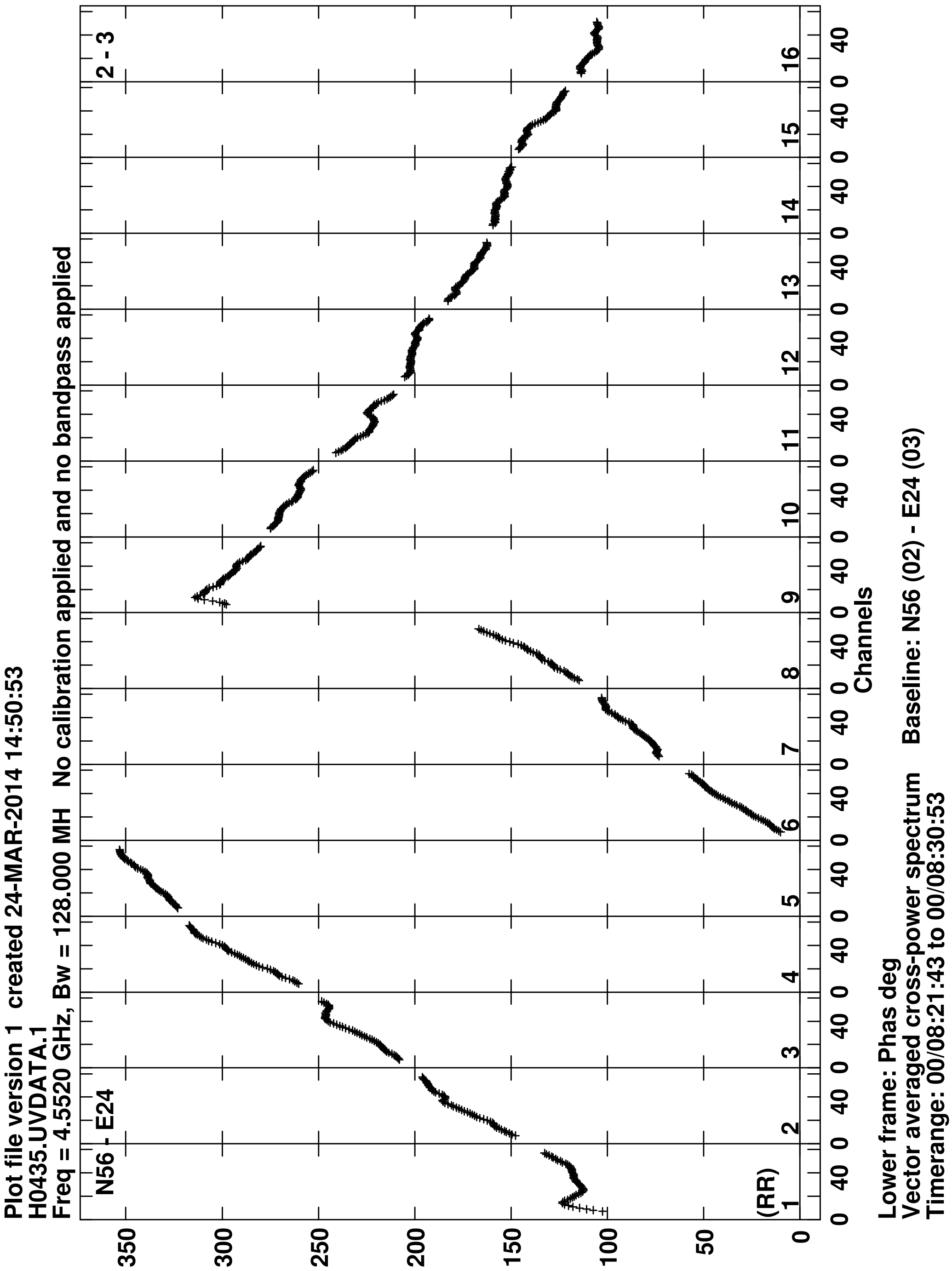

Figure 2.2: This is a POSSM plot of the October HE0435-1223 dataset before fringe fitting. The plot features the flux received by baseline 2-3 during the time when 3C138 was observed.

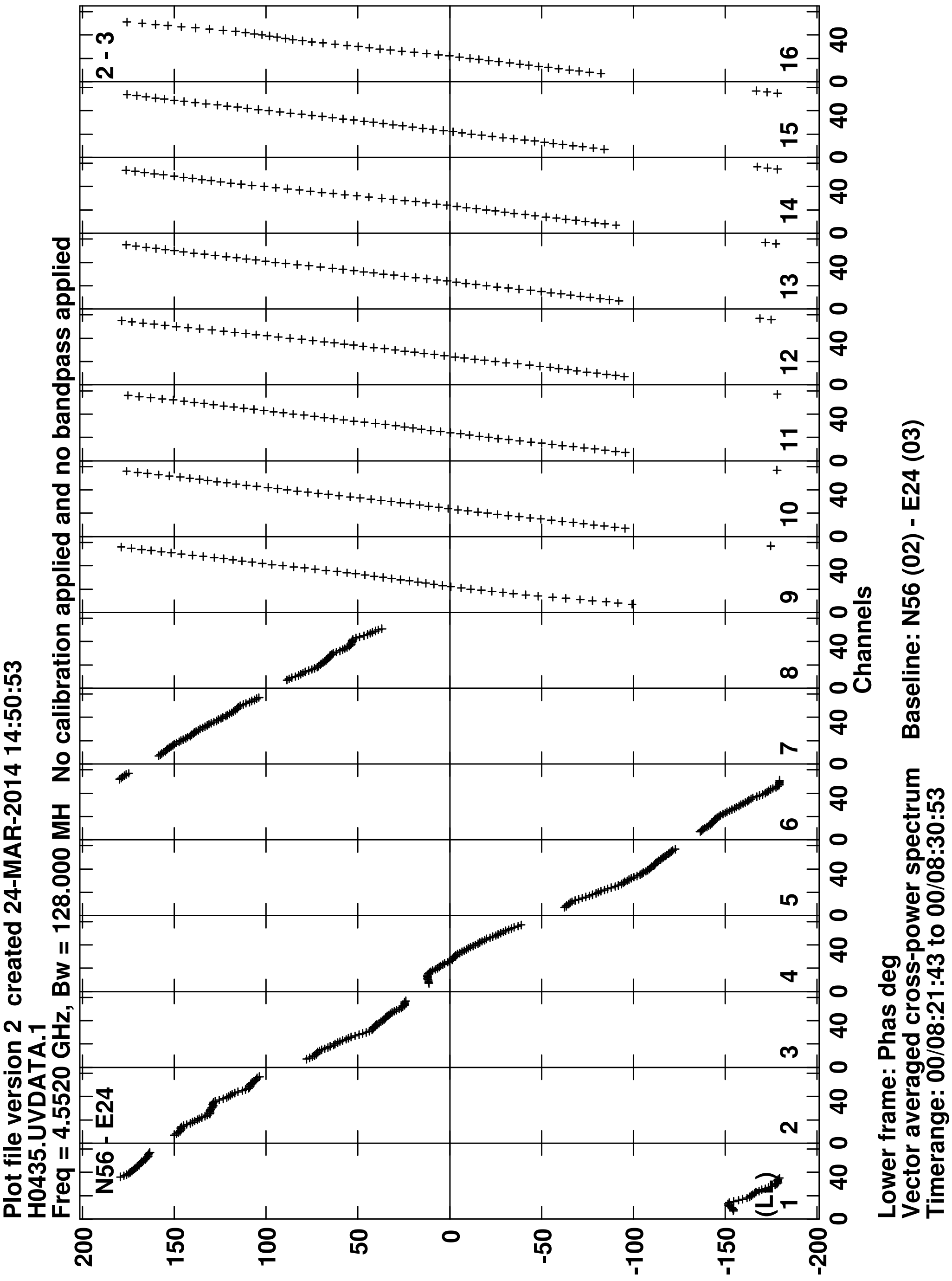

Figure 2.3: This is a POSSM plot of the October HE0435-1223 dataset before fringe fitting. The plot features the flux received by baseline 2-3 during the time when 3C138 was observed.

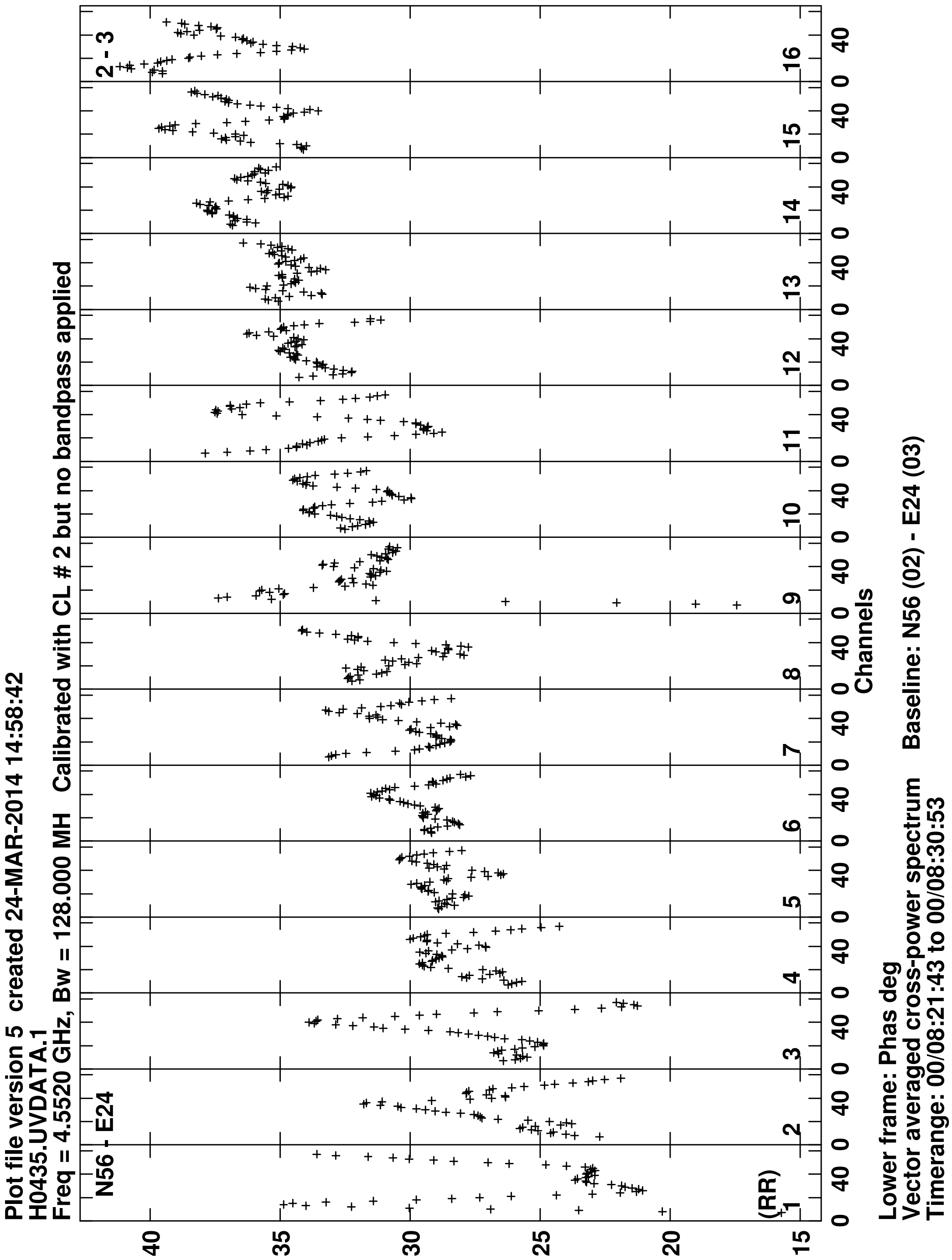

Figure 2.4: This is a POSSM plot of the October HE0435-1223 dataset after fringe fitting. The plot features the flux received by baseline 2-3 during the time when 3C138 was observed

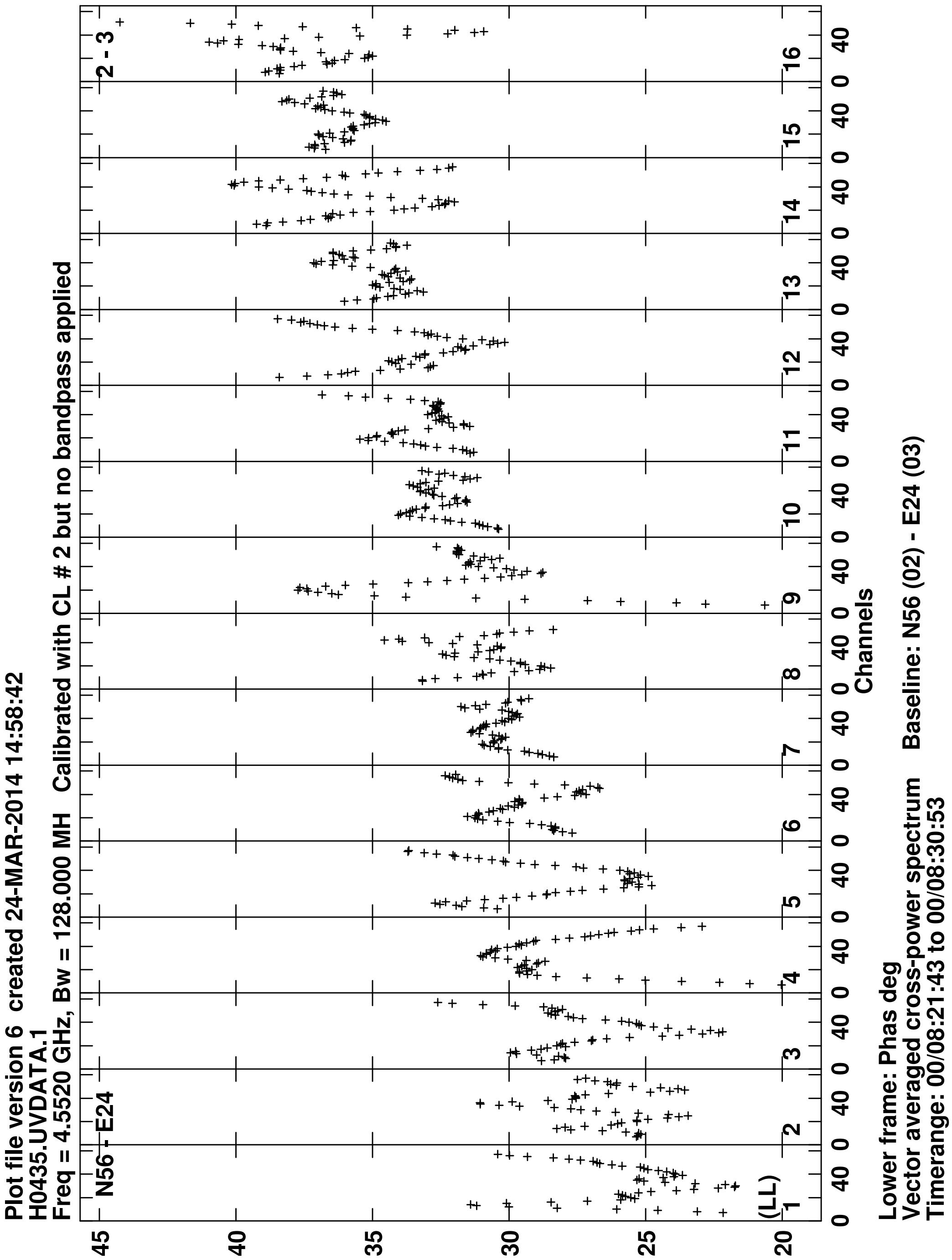

Figure 2.5: This is a POSSM plot of the October HE0435-1223 dataset after fringe fitting. The plot features the flux received by baseline 2-3 during the time when 3C138 was observed

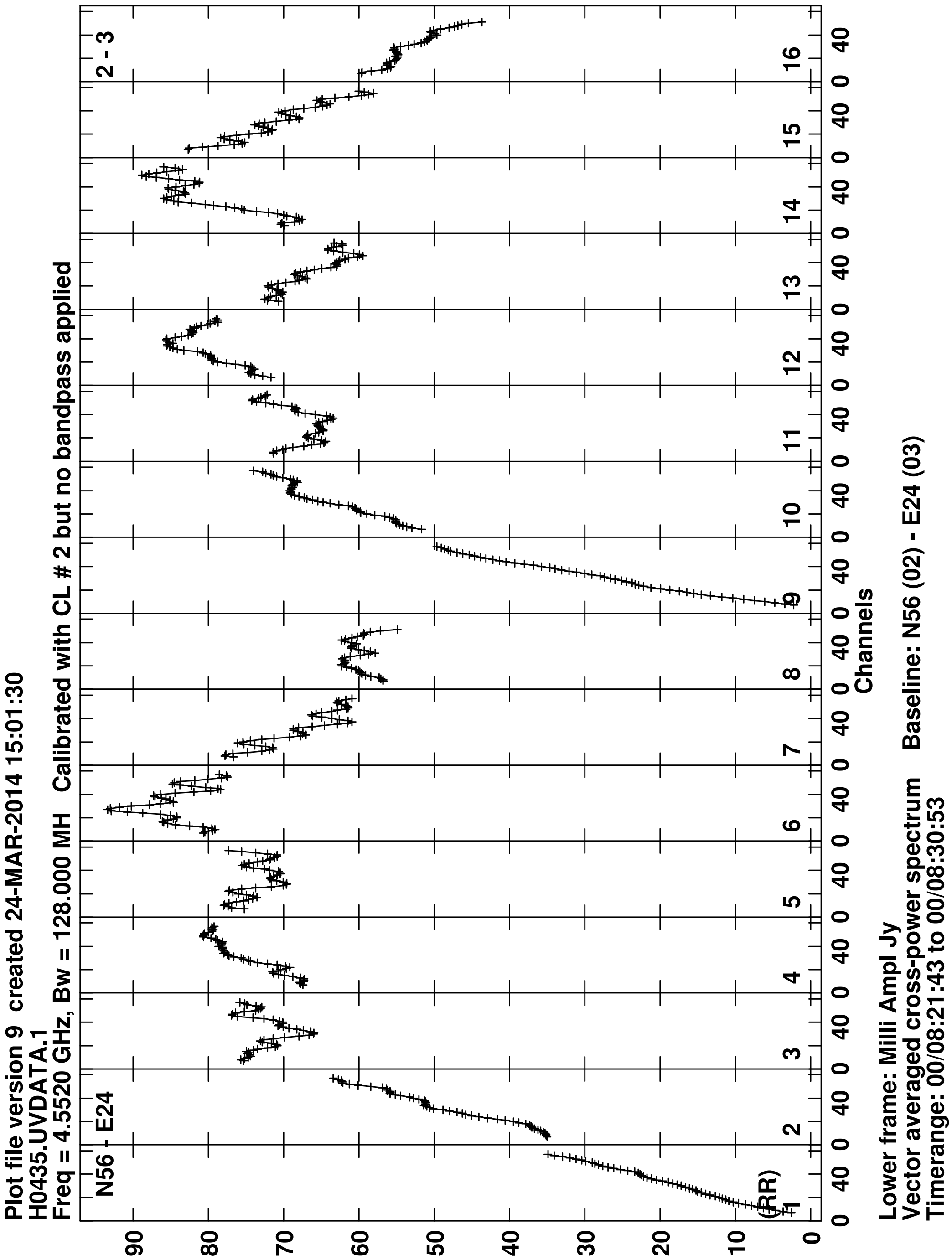

Figure 2.6: This is a POSSM plot of the October HE0435-1223 dataset before bandpass calibration. The plot features the flux received by baseline 2-3 during the time when 3C138 was observed

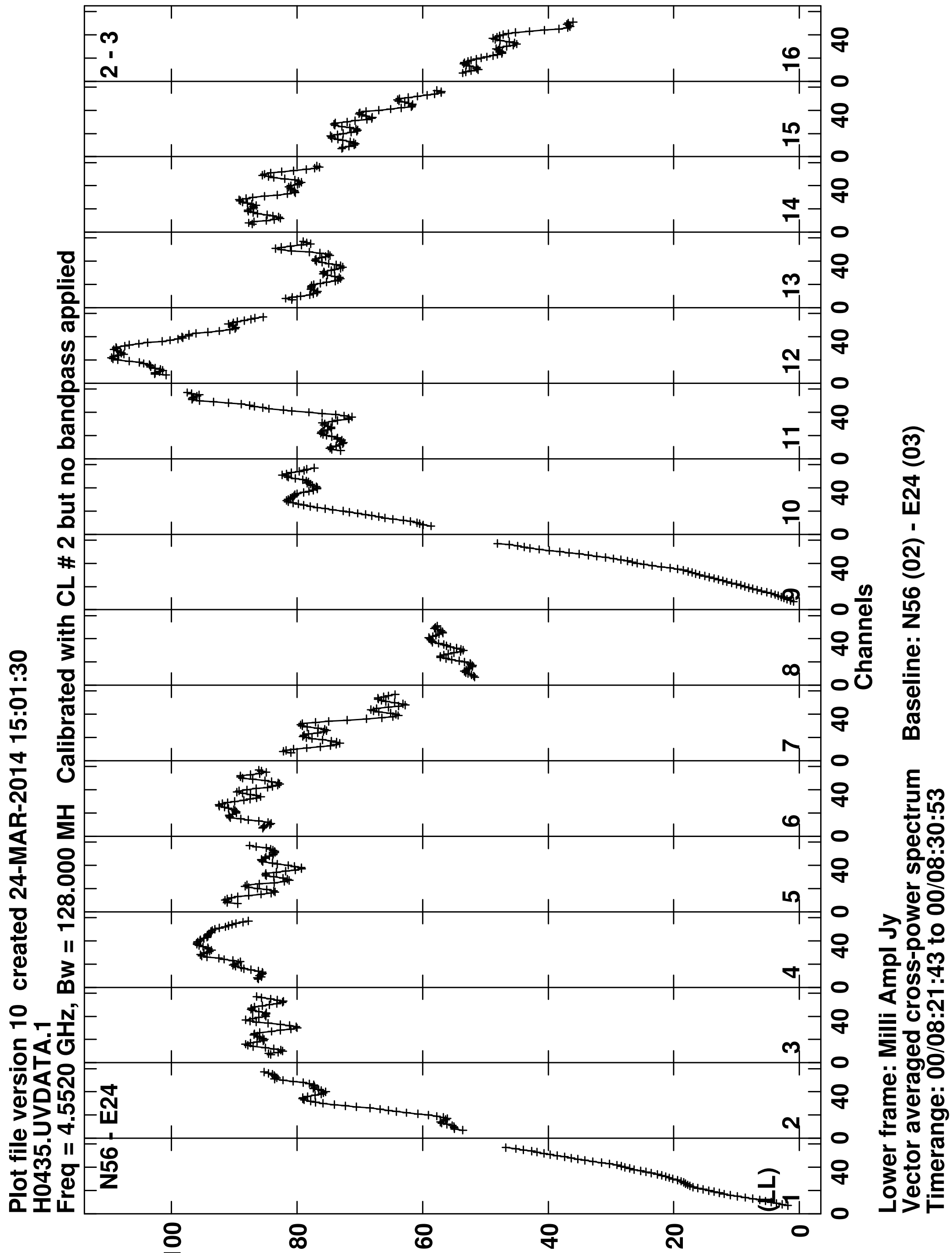

Figure 2.7: This is a POSSM plot of the October HE0435-1223 dataset before bandpass calibration. The plot features the flux received by baseline 2-3 during the time when 3C138 was observed

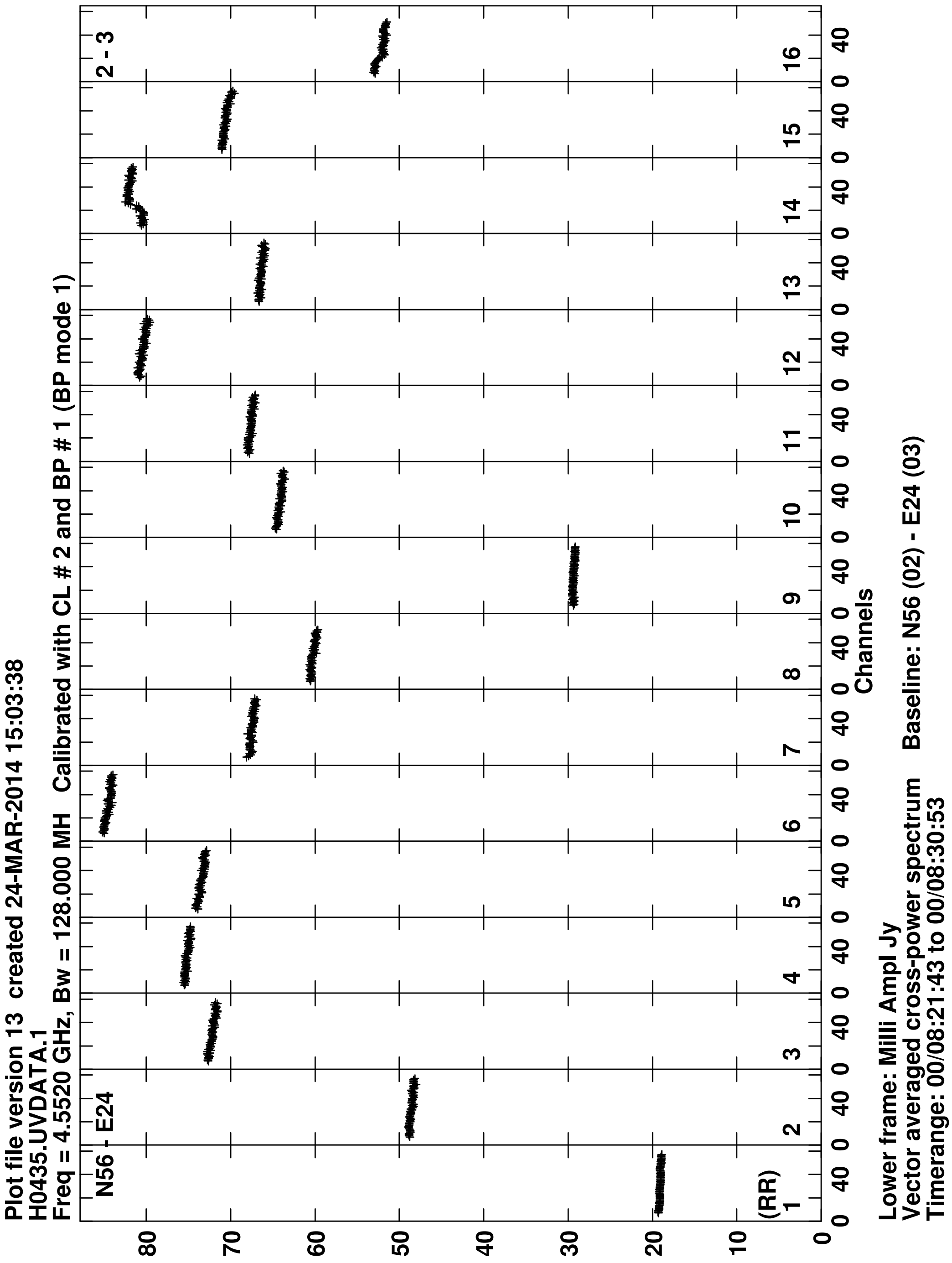

Figure 2.8: This is a POSSM plot of the October HE0435-1223 dataset after bandpass calibration. The plot features the flux received by baseline 2-3 during the time when 3C138 was observed. The offsets are later corrected by amplitude self-calibration on the phase calibrator.

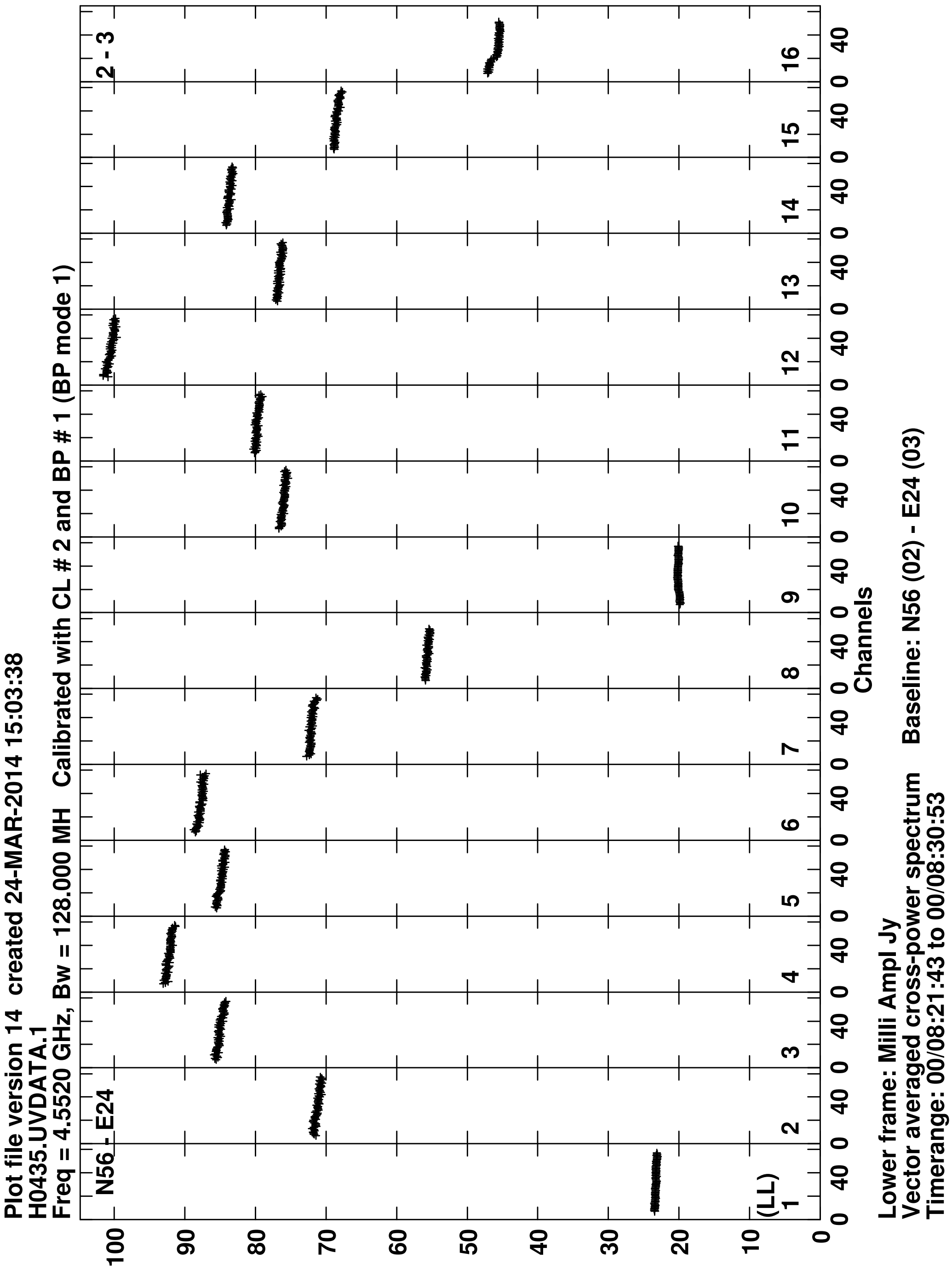

Figure 2.9: This is a POSSM plot of the October HE0435-1223 dataset after bandpass calibration. The plot features the flux received by baseline 2-3 during the time when 3C138 was observed.

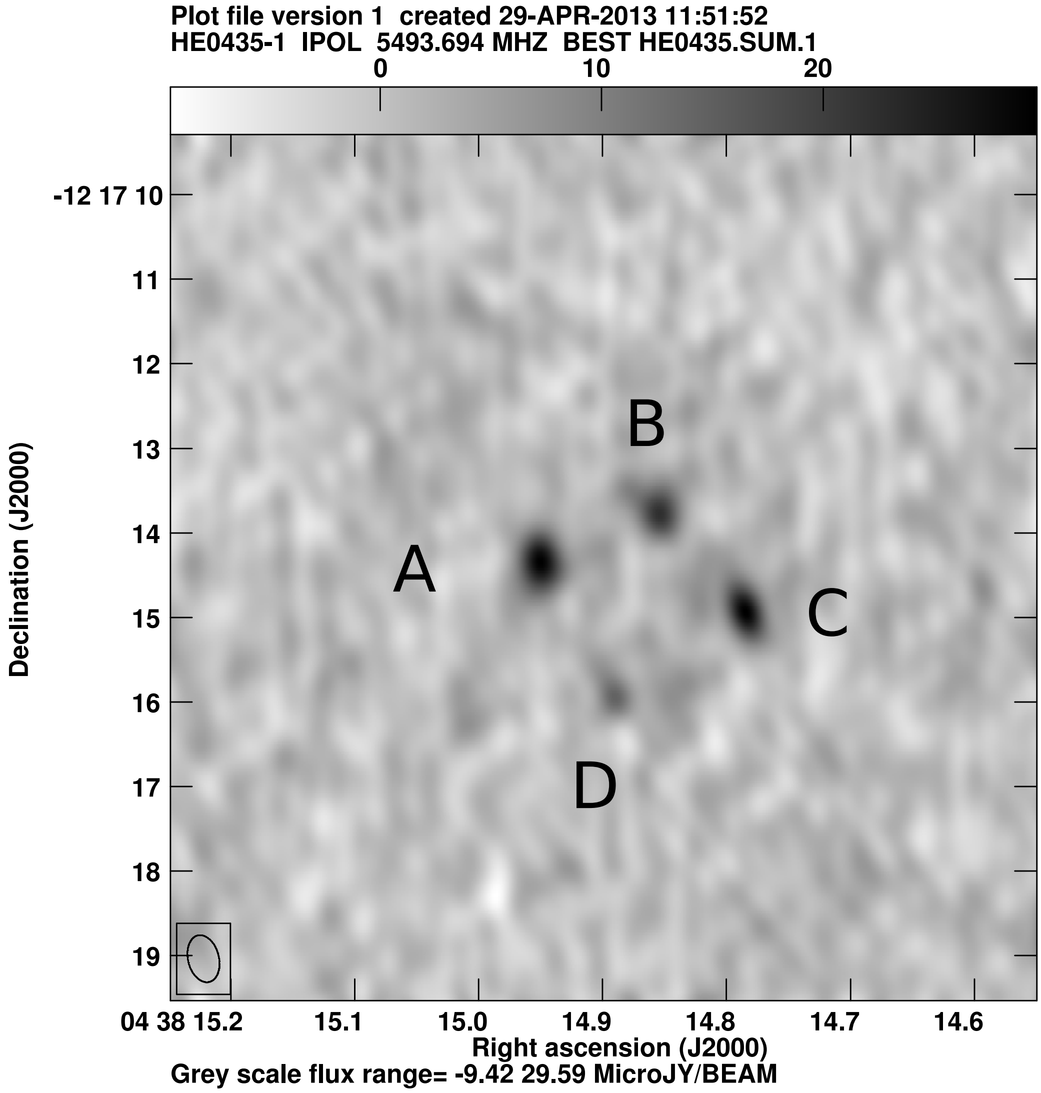

Figure 2.10: This is the radio map of the combined datasets of HE0435-1223. The images are labelled A, B, C and D in clockwise fashion, starting with the left-most image as image A. The rms noise on this image is 2.12×10^{-6}Jy. The ellipse at the lower left corner shows the beam size and shape; the beam width is 0.4" along the right ascension axis and 0.6" along the declination axis.

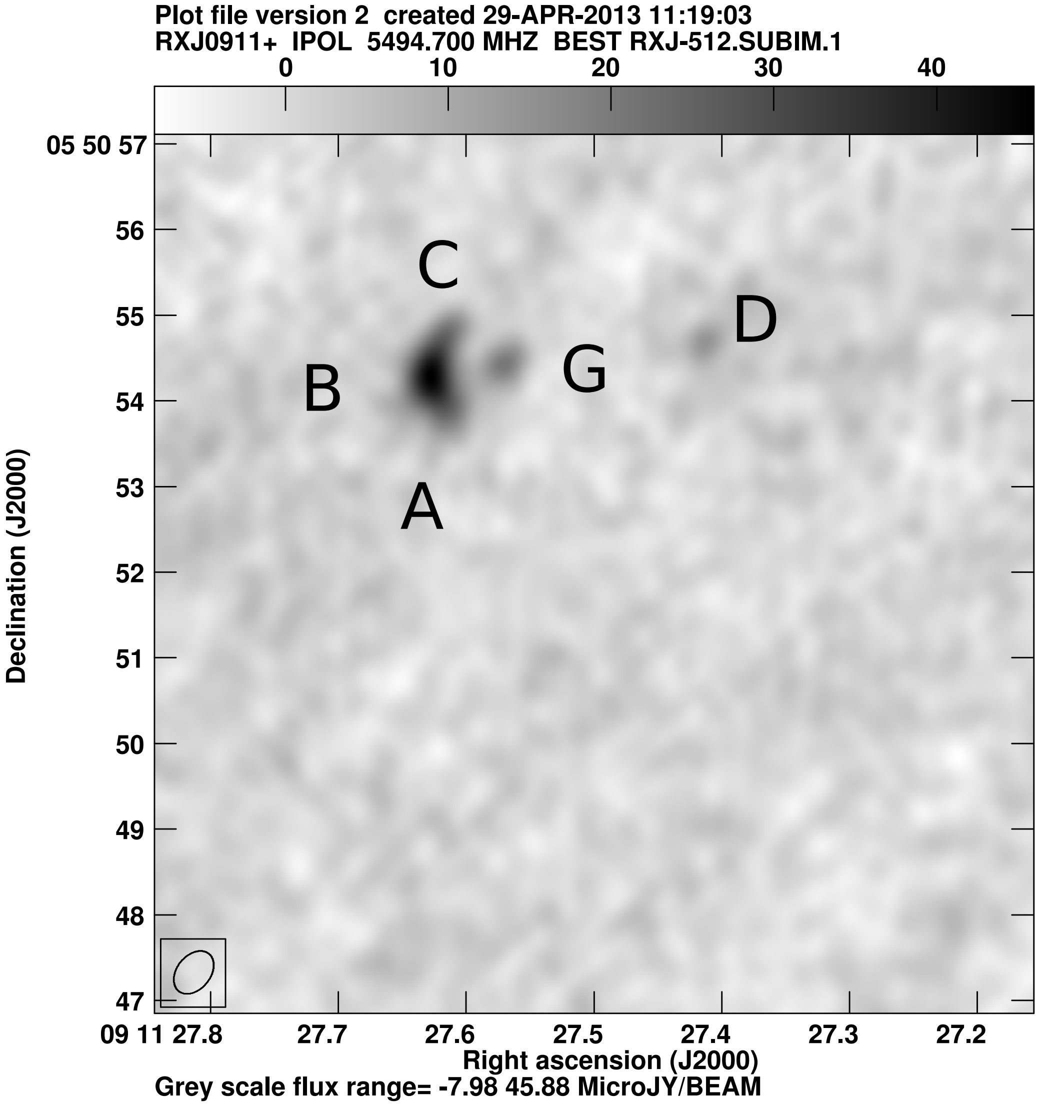

Figure 2.11: This is the radio map of the combined datasets of RXJ0911+0551. The images are labelled A, B, C and D in a clockwise manner, with image A being the bottom image in the arc, the lens galaxy labelled G is between the arc and image D. The rms noise for this image is 2.21×10^{-6}Jy. The ellipse at the lower left corner shows the beam size and shape; the beam width is 0.5" along the right ascension axis and 0.6" along the declination axis.

Chapter 3

Results

This chapter begins with a brief summary of the prior work published on HE0435-1223 and RXJ0911+0551, then proceeds to an examination of the radio images obtained.

3.1 HE0435-1223

This lens system was first found as a high probability lensing candidate in the Hamburg/ESO digital objective prism survey. It was confirmed as a lens system in 2002 [Wisotzki et al., 2002] by spectroscopic observation. The images form a classic Einstein cross, an arrangement where the four images form the points of a cross or cruciform; this occurs when the lensed object is directly behind the lensing galaxy. The astromety and photometric data from previous studies is presented in this section in Tables 3.1-3.7

The maximum separation between images is 2.6 arcseconds and the lensed galaxy is at redshift $z = 1.689$. In [Wisotzki et al., 2002], the redshift of the lensing galaxy is estimated to be $0.3 < z < 0.4$ based on their lens model and the observed colours. Later, the redshift of the lensing galaxy was measured [Morgan et al., 2005] to be $z = 0.4541$. The time delays were predicted [Wisotzki et al., 2002] to be 10 days because an Einstein cross is highly symmetric, so there is little difference in path length between the images. Two years of optical photometry of HE0435-1223 were performed to find the time delays [Kochanek et al., 2006], with $\Delta t_{AD} = -14.37 \pm 0.85$, $\Delta t_{AB} = -8.00 \pm 0.82$ and $\Delta t_{AC} = -2.10 \pm 0.78$ days.

Microlensing is believed by [Wisotzki et al., 2003] to be a factor in HE0435-1223 because there is a significant difference in the continuum fluxes and the emission line fluxes of the images. The emission line regions of quasars are believed to be larger than the Einstein radius of stellar mass lenses, so any stellar lensing is smeared out, whereas the continuum-emitting region is orders of magnitude smaller and is known to be subject to microlensing.

An analysis of the environment around the lens system was performed [Morgan et al., 2005], which identified a number of nearby galaxies. In particular galaxy G12 was found, which has the same redshift as the lensing galaxy and a V-band magnitude of 21.182 ± 0.018. Its position is in Table 3.5. However, they found that the shear of their models (with $0.01 < \gamma < 0.14$) was pointing in a peculiar manner. It was not pointing towards the galaxies thought most likely to cause it, but actually around 30 degrees away from G12. Therefore, either the macromodel needed to be more complicated or the macromodel was correct but there are perturbing effects.

In the paper [Ricci et al., 2011], HE0435-1223 was observed over two periods. Between these periods, all four components decreased in magnitude and changed colour by the same amount. Because the time delays are short and microlensing leads to uncorrelated flux changes, the observed changes are caused by intrinsic variations in the quasar.

Recently, research [Fadely and Keeton, 2012b] indicates that models with substructure have three orders of magnitude higher evidence values than those without, therefore there is strong evidence for substructure in HE0435-1223. They began with using Bayesian evidence to compare smooth models with those that added truncated, isothermal clumps near the images. The observed A/C flux ratio could not be reproduced by macroscopic, smooth models but it could be accounted for by adding a clump near image A. Next a full population of subhalos was modelled using a mass function consistent with CDM, then varying the abundance of substructure and looking at the Bayesian evidence. In doing so, [Fadely and Keeton, 2012b] inferred the fraction of substructure to have a lower bound of $f_{sub} > 0.00077$, which is consistent with, but weaker than, other lensing measurements. It was also found [Fadely and Keeton, 2012b] by comparing to the Bayes factor that finding the best value of χ^2 may be an unreliable indicator of evidence in HE0435-1223, but suggest this may be caused by not fully marginalising the macromodel.

Image	g	r	i
A	19.00	18.44	17.95
B	19.51	18.95	18.43
C	19.60	19.01	18.47
D	19.64	19.10	18.66

Table 3.1: The magnitudes relative to a nearby reference star for the components of HE0435-1223 from [Wisotzki et al., 2002].

Component	$\Delta R.A.[arcsec]$	$\Delta Dec[arcsec]$
A	0.000	0.000
B	-1.483 ±0.002	0.567 ±0.002
C	-2.488 ±0.003	-0.589 ±0.002
D	-0.951 ±0.001	-1.620 ±0.001
G	-1.15 ±0.05	-0.51 ±0.05

Table 3.2: Astrometry for HE0435-1223 from [Wisotzki et al., 2002], where component G is the lensing galaxy. The positions are relative to image A.

Image	V	g	r
A	18.34	18.50	18.16
B	18.88	19.03	18.70
C	18.96	19.15	18.77
D	18.90	19.07	18.72

Table 3.3: The Vega magnitudes for the components of HE0435-1223 in Johnson V and SDSS g and r bands from [Wisotzki et al., 2003].

Component	$\Delta R.A.$(“)	ΔDec(“)	V/V_A	I/I_A
A	=0	=0	=1	=1
B	-1.4772 ±0.002	0.5532 ±0.002	0.607 ±0.016	0.621 ±0.003
C	-2.4687 ±0.002	-0.6033 ±0.002	0.579 ±0.012	0.617 ±0.003
D	-0.9377 ±0.002	-1.1687 ±0.002	0.557 ±0.010	0.516 ±0.003
G	-1.1687 ±0.002	-0.5723 ±0.002	-	-

Table 3.4: The HST astrometry and fluxes for the components of the lens system HE0435-1223 in the V and I bands [Morgan et al., 2005], where component G is the lensing galaxy. The positions and photometric measurements are relative to image A.

Object	$\Delta R.A.[arcsec]$	$\Delta Dec.[arcsec]$
G12	-8.96	3.66

Table 3.5: Astrometry of galaxy G12 identified in [Morgan et al., 2005] relative to the position of HE0435-1223.

Component	$\Delta R.A.$(“)	ΔDec(“)	V	I
A	=0	=0	18.41 ±0.03	17.84 ±0.02
B	+1.476 ±0.003	+0.553 ±0.001	18.99 ±0.07	18.39 ±0.04
C	+2.467 ±0.002	-0.603 ±0.004	19.07 ±0.06	18.41 ±0.02
D	+0.939 ±0.002	-1.614 ±0.001	19.12 ±0.04	18.62 ±0.04
G	+1.165 ±0.002	-0.573 ±0.002	-	-

Table 3.6: HST Astrometry and photometry of HE0435-1223 in Vega magnitudes from [Kochanek et al., 2006], where component G is the lensing galaxy.

Component	$\Delta R.A.$(“)	ΔDec(“)	R	K	L’
A	-1.165 ±0.003	0.573 ±0.003	1.751 ±0.098	1.837 ±0.086	1.706 ±0.085
B	+0.311 ±0.004	+1.126 ±0.004	0.998 ±0.037	1.271 ±0.063	0.991 ±0.065
C	+1.302 ±0.005	-0.030 ±0.005	=1	=1	=1
D	-0.226 ±0.003	-1.041 ±0.003	0.851 ±0.049	0.745 ±0.049	0.809 ±0.090
G	=0 ±0.002	=0 ±0.002	-	-	-

Table 3.7: Astrometry and photometry of HE0435-1223 from [Fadely and Keeton, 2012b]. The positions are relative to the lensing galaxy G and the photometric measurements are relative to C.

3.2 RXJ0911+0551

The lens system RXJ0911+0551 was discovered in 1997 via X-ray observation and was confirmed to be a lens system through follow-up optical imaging [Bade et al., 1997]. It is an example of a lens where the source is close to the inner edge of the cusp of the caustic in the lens plane, which results in three of the images (images A, B and C) lying close to one another in an arc, while image D is alone on the opposite side of the lens galaxy G. Tables 3.8 and 3.9 show the astrometry and photometric data from previous studies of this system. The system has a maximum separation of 3.1". The quasar is at redshift 2.8 and the lens galaxy was found to be $z = 0.6 - 0.8$ by [Burud et al., 1998], who also noted that the lens galaxy has an ellipticity of 0.075. Later, the redshift of the lensing galaxy was pinned down at $z = 0.77$ [Hjorth et al., 2002].

An odd feature of this system is that it has an abnormally large external shear, approximately 0.15 [Burud et al., 1998]. This is believed to be caused by a nearby cluster 38 arcsec south-west of the lens at redshift 0.7 ± 0.1 [Tortora et al., 2004] and a mass of 2.3×10^{18} solar masses in its virial radius [Morgan et al., 2001]. Later work indicated that the shear may be greater, by using the time delay observed from the Nordic Optical Telescope between image D and the composite image comprised of A, B and C, which was 146 ± 8 days [Hjorth et al., 2002]. This was much shorter than predicted from simple models and implied that the shear is $0.20 < \gamma < 0.28$. Regardless of this issue, RXJ0911+0551 was viewed as a good lens to obtain time delays on because the quasar is highly variable, which enables accurate measurement of the time delay.

RXJ0911+0551 was used [Chartas et al., 2001] to test whether X-ray observations of a lens system over a protracted period of time could produce accurate time delays. During the observation, there was an X-ray flare in image B. This could not have been microlensing because of its short duration; therefore, it was an intrinsic variation, which was used to produce an accurate time delay in agreement with prior results. The RXJ0911+0551 time delay was used in conjunction with the PG1115+080 time delays to estimate $H_0 = 56 \pm 23 kms^{-1} Mpc^{-1}$ [Tortora et al., 2004]. However, [Eulaers and Magain, 2011] found that there are two possible time delays between the combined A+B+C image and image D Δt_{AB} 146 or Δt_{AB} 157. They concluded that this was probably due to the algorithms calculating the time delays being highly dependent on a small number of events in the light curve, so the problem could be resolved by longer observation periods.

There may be some evidence of microlensing in the system from differences between the images' emission lines and continuum fluxes [Anguita et al., 2008], with the ratio of A+B+C to image D being 5.9 for continuum emission and 7.7 for emission lines. This was concluded [Anguita et al., 2008] to be due to microlensing in A+B+C. Since A and C are saddle points, they are more likely to be demagnified by microlensing events [Schechter and Wambsganss, 2002]. Another event suspected of being caused by microlensing was during X-ray observations of the lens [Morgan et al., 2001], where compared to previous optical images, image C was dimmer by a factor of 6 in the X-ray with respect to images A and B. It is rare for microlensing to be this strong, and without further evidence, [Morgan et al., 2001] no conclusions could be made.

RXJ0911+0551 shows evidence for differential extinction between images [Keeton et al., 2003], in CASTLES image A has colours $V - H = 1.24 \pm 0.04$ and $I - H = 0.79 \pm 0.04$ while images B and C both have $V - H = 1.54 \pm 0.05$ and $I - H = 1.01 \pm 0.04$. Colour difference is likely from dust in the lens galaxy. The lens appears to have a flux ratio anomaly at optical/near-IR. In theory $R_{cusp} = 0$ as the source approaches the cusp, but for RXJ0911+0551 R_{cusp} for A, B and C is 0.23 ± 0.06 and the model predicts that it should be 0.00. However, there is a need to be cautious when making conclusions about the presence of substructure based on R_{cusp} alone [Bradač et al., 2004] because of difficulties in detailed modelling and if the lens galaxy has a disc, that can destroy the cusp relation. These effects can produce, in models without substructure, strong violations in the cusp relation. However, most lens galaxies are elliptical, because elliptical galaxies tend to be more massive than spiral galaxies.

	A	B	C	D	G
Δx(“)	0.000 ±0.004	-0.259 ±0.007	0.013 ±0.008	2.935 ±0.002	0.709 ±0.026
Δy(“)	0.000 ±0.008	0.402 ±0.006	0.946 ±0.008	0.785 ±0.003	0.507 ±0.046
K-band	=1	0.965 ±0.013	0.544 ±0.025	0.458 ±0.004	-
J-band	=1	0.885 ±0.003	0.496 ±0.005	0.412 ±0.005	-
I-band	=1	0.680 ±0.013	0.398 ±0.002	0.420 ±0.003	-
V-band	=1	0.587 ±0.009	0.334 ±0.004	0.413 ±0.006	-
U-band	=1	0.590 ±0.013	0.285 ±0.007	0.393 ±0.004	-
Mag	-4.45	+8.59	-3.70	+1.79	-

Table 3.8: Astrometry, photometry and best-fit model magnifications of RXJ0911+0551 from [Burud et al., 1998]. The positions and fluxes are measured relative to image A. G is the lensing galaxy.

Triplet	Data	Model
BCD	0.45 ±0.05	0.44
ACD	0.59 ±0.04	0.67
ABD	0.14 ±0.06	0.38
ABC	0.23 ±0.06	0.00

Table 3.9: The values of R_{cusp} for the lens system RXJ0911+0551 from the data and those predicted by the model [Keeton et al., 2003]

3.3 Analysis of the radio images

Now that the radio maps of the lens systems are created, we require the fluxes of the images. To do so, I fit Gaussian distributions to the images. However, it is necessary to be able to check whether the values obtained are accurate. Hence, I modelled the fluxes via two separate methods: the first is fitting to the image plane by using the *JMFIT* function in AIPS, the second is to fit to the data in the uv-plane using Difmap. Theoretically, fitting to the uv data should be more accurate because it is not subject to CLEAN errors, but Difmap does not produce error bounds for the flux or the position, so we shall use the fluxes from Difmap to test the fluxes obtained through *JMFIT*. In both processes, the input parameters are nearly the same; the Gaussian is spherical, the width of the Gaussian is set to be the width of the clean beam, the position of the components is set to wherever looks best by eye and the initial peak flux of the Gaussian is set to be the flux at the components initial position. The position and flux of the components is allowed to vary, and is modelled to the data by a least-squares method. In both cases, it returns the intergrated flux as the flux of the images. In the Table 3.10 and 3.11 are the results.

	A	B	C	D
$\Delta R.A.$(“)	$= 0 \pm 0.011$	-1.435 ± 0.015	-2.479 ± 0.012	-0.886 ± 0.026
$\Delta Dec.$(“)	$= 0 \pm 0.05$	-0.614 ± 0.021	0.564 ± 0.017	1.537 ± 0.037
JMFIT flux (μJy)	34.3 ± 2.2	25.2 ± 2.2	31.8 ± 2.2	14.3 ± 2.2
Difmap flux (μJy)	32.0	25.6	33.0	16.6

Table 3.10: Astrometry and photometry of HE0435-1223 from the radio map. The postions of the images are relative to image A.

	A	B	C	D	G
$\Delta R.A.$(“)	$= 0 \pm 0.016$	0.239 ± 0.10	0.089 ± 0.017	-3.036 ± 0.030	-0.639 ± 0.021
$\Delta Dec.$(“)	$= 0 \pm 0.017$	0.350 ± 0.011	0.815 ± 0.018	0.782 ± 0.032	0.530 ± 0.032
JMFIT flux (μJy)	27.8 ± 2.3	45.3 ± 2.3	26.7 ± 2.3	15.0 ± 2.2	21.4 ± 2.3
Difmap flux (μJy)	25.4	34.5	20.6	12.4	19.4

Table 3.11: Astrometry and photometry of RXJ0911+0551 from the radio map. The positions of the components are relative to image A.

In both systems, we can discount the possibility that any discrepancy in fluxes between the radio and the optical observation is because of the intrinsic variability in the quasar. This is because the time delay in HE0435-1223 and the delays between the images A, B and C of RXJ0911+0551 are short, on the order of a few days. If the quasar brightened due to the quasar intensifying, then the other images would quickly follow suit. Moreover, each lens had at least two observation periods with a month between them, so the effect would be noticed in the second observation.

For HE0435-1223 there is a close agreement between the fluxes from Difmap and those from *JMFIT*, all the fluxes are within two sigma of each other, therefore, the *JMFIT* fluxes can be used. However, for RXJ0911+0551 the fluxes do not match up so well: the Difmap flux for image B is 4.7σ less than the *JMFIT* flux and the rest of the images are within 3σ. The different fluxes for image D and for the lensing galaxy G agree well, so the difference between the two methods probably arose because of the difficulty in consistently fitting three Gaussian components to the merged ABC arc. To determine the most accurate flux would require methods beyond the scope of this work, possibly using Markov chain Monte Carlo methods to fit directly to the uv data and determine the errors [Hezaveh et al., 2013b]. Therefore, the analysis of RXJ0911+0551 will take into account both fluxes, except when modelling where the *JMFIT* fluxes only with be used, because their errors are known.

The cusp relation R_{cusp} for the triplet ABC in theory for a cusp should be zero. For the Difmap fluxes $R_{cusp} = 0.143$ and for the *JMFIT* fluxes $R_{cusp} = 0.092 \pm 0.018$, both of which are considerably lower than the previous value of $R_{cusp} = 0.23 \pm 0.06$ from [Keeton et al., 2003].

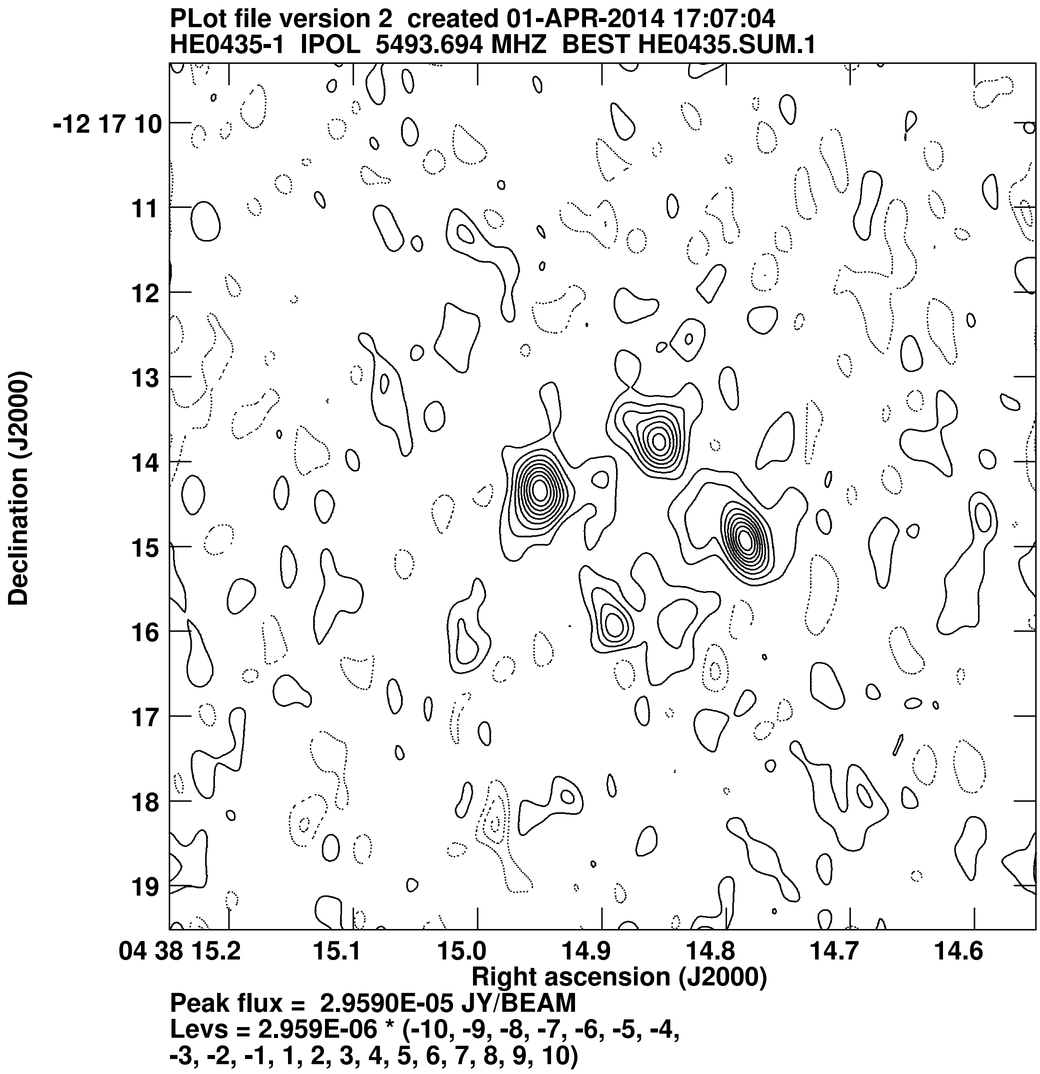

Figure 3.1: The CLEAN image of HE0435-1223.

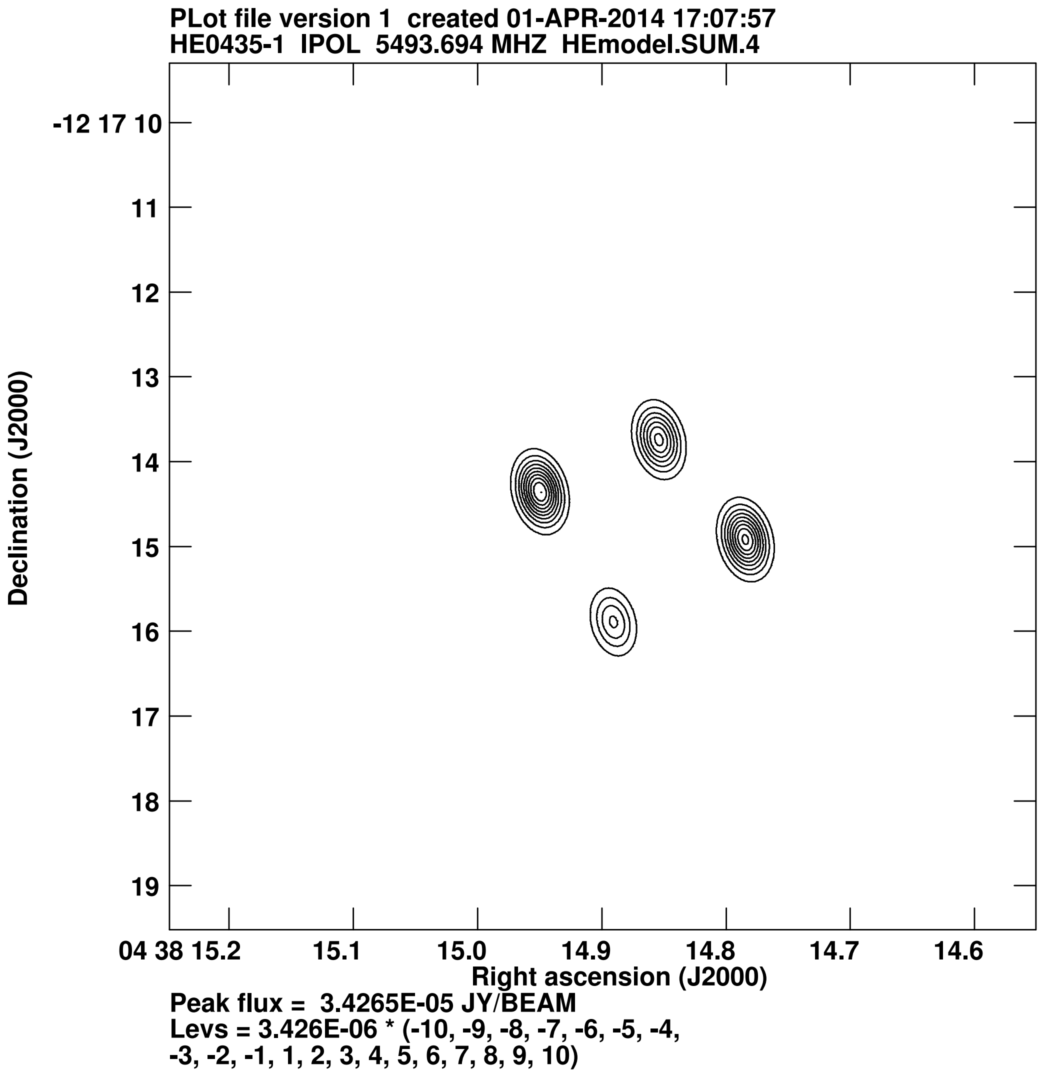

Figure 3.2: The JMFIT model of HE0435-1223

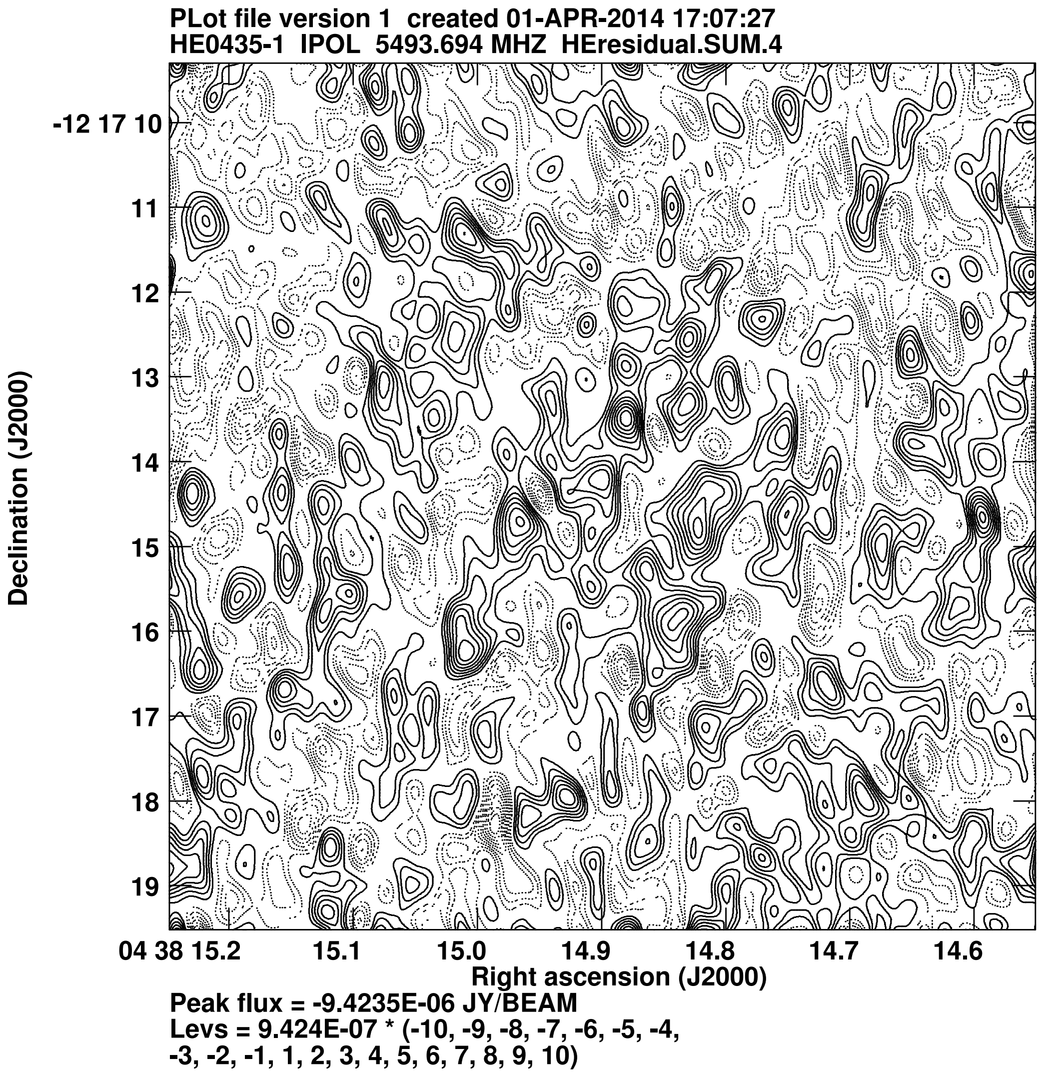

Figure 3.3: The residual map of HE0435-1223 when the JMFIT model is removed from the CLEAN image.

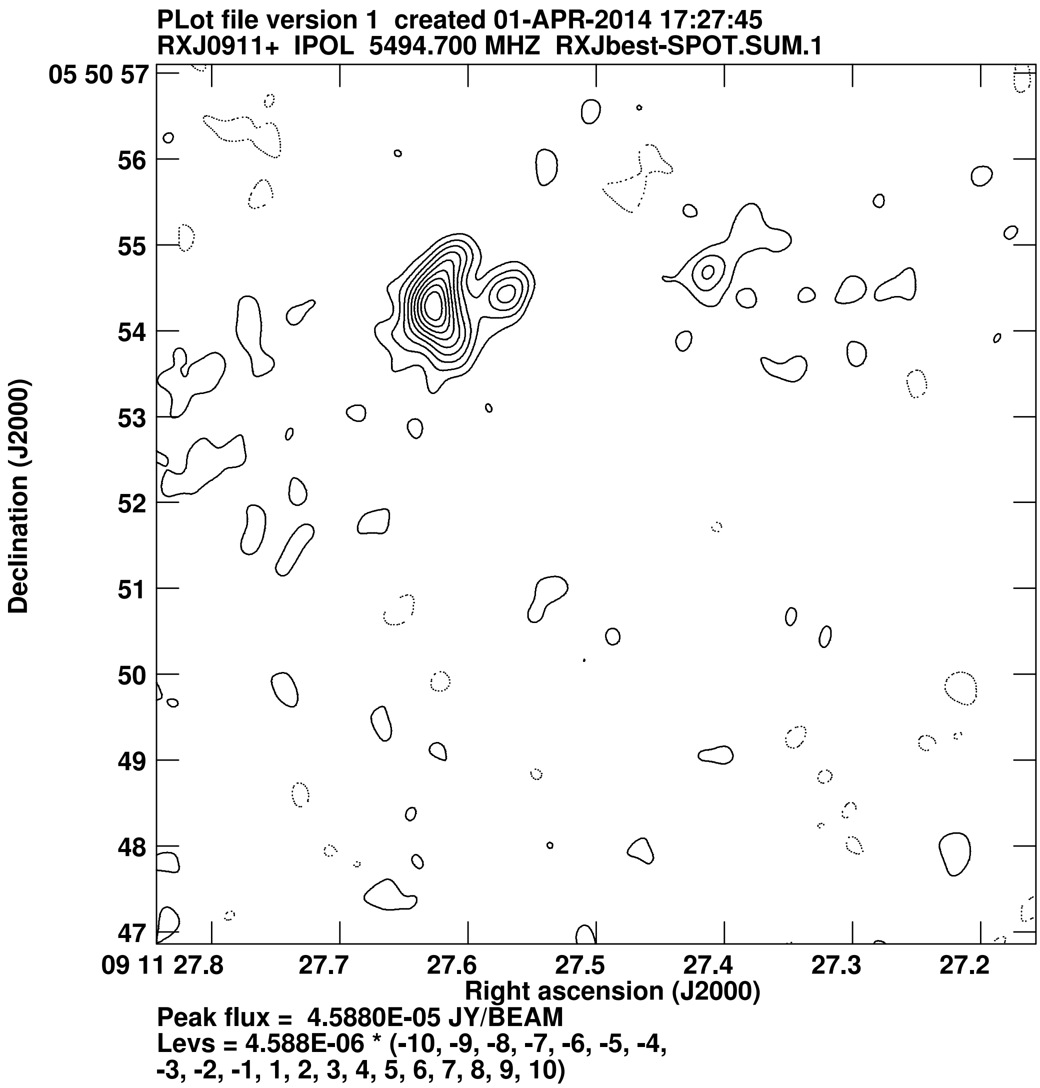

Figure 3.4: The CLEAN image of RXJ0911+0551

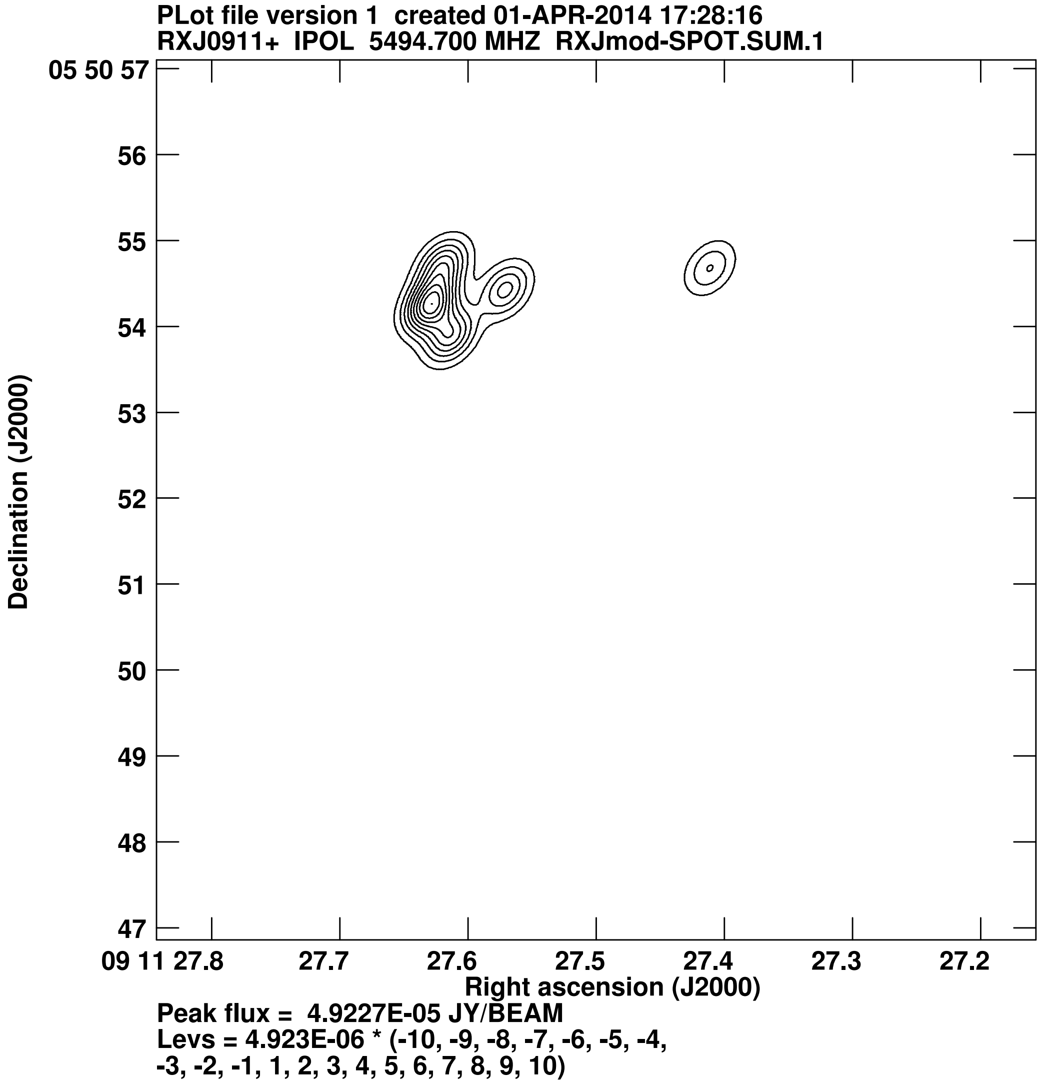

Figure 3.5: The JMFIT model of RXJ0911+0551

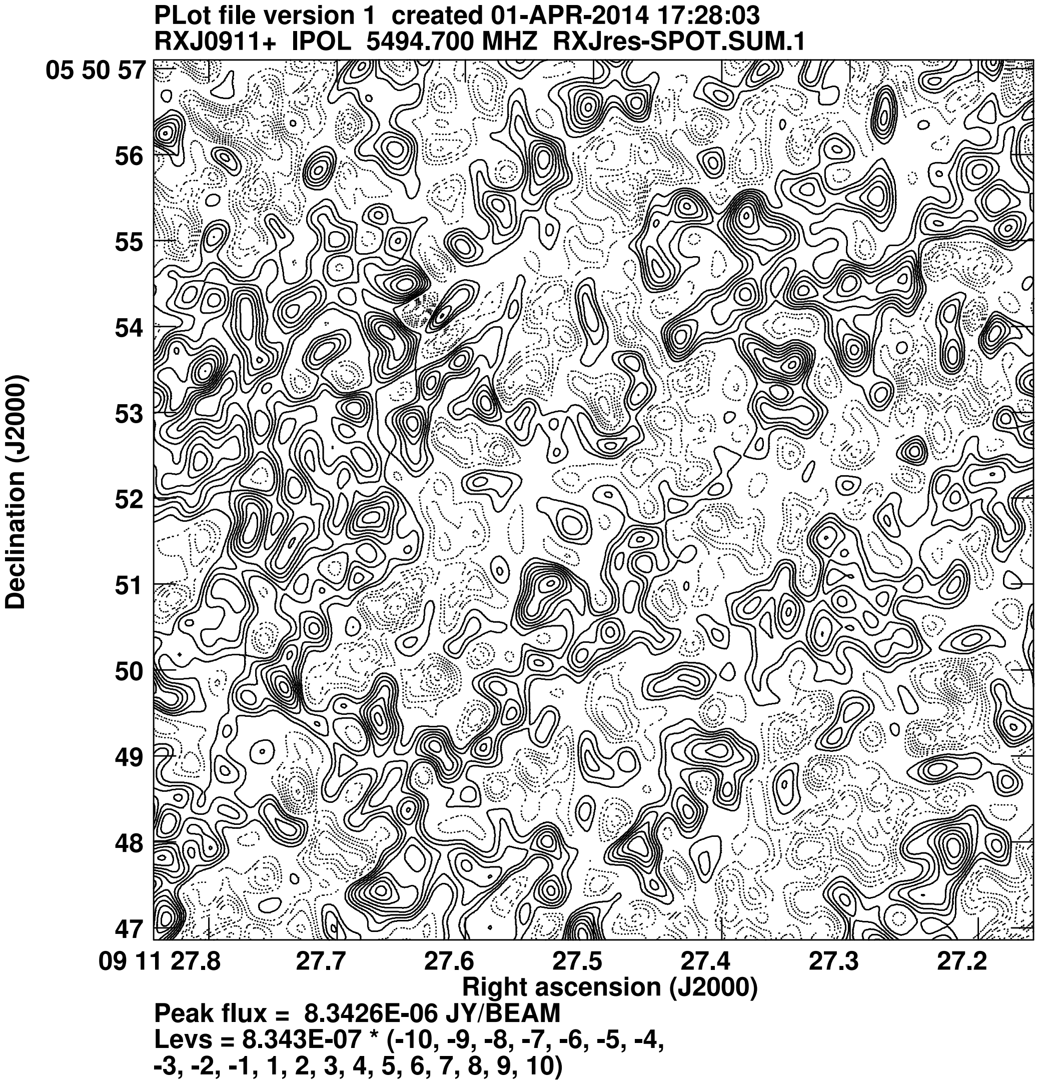

Figure 3.6: The residual map of RXJ0911+0551 when the JMFIT model is removed from the CLEAN image.

Chapter 4

Interpretation

This chapter compares the radio fluxes to those obtained by previous authors, before presenting some new smooth models of both systems using the radio positions and fluxes and contrasting them with older models. The chapter ends with an examination of whether there is evidence of substructure in the observations.

4.1 Flux comparison

The first piece of analysis to perform is to look for differences between the radio and the shorter wavelength fluxes. Radio waves are unaffected by dust extinction and by microlensing, because the radio emitting region of the quasar is much larger than the typical Einstein radius of the stars in the lensing galaxy. So by comparing with previous results, the effect of microlensing and extinction can be seen. In this way, only the effect of substructure on the flux ratios can be seen.

	A	B	C	D
Radio flux	=1	0.74 ± 0.11	0.93 ± 0.13	0.42 ± 0.09
V-band [Morgan et al., 2005]	=1	0.607 ± 0.016	0.579 ± 0.012	0.557 ± 0.010
I-band [Morgan et al., 2005]	=1	0.621 ± 0.003	0.617 ± 0.003	0.516 ± 0.003
R-band [Fadely and Keeton, 2012b]	=1	0.570 ± 0.056	0.571 ± 0.034	0.486 ± 0.058
K-band [Fadely and Keeton, 2012b]	=1	0.692 ± 0.070	0.544 ± 0.027	0.406 ± 0.047
L'-band [Fadely and Keeton, 2012b]	=1	0.581 ± 0.070	0.586 ± 0.031	0.471 ± 0.081

Table 4.1: Table of the fluxes of the images of HE0435-1223.

	A	B	C	D
Radio flux (JMFIT)	=1	1.63 ± 0.24	0.96 ± 0.15	0.54 ± 0.14
Radio flux (Difmap)	=1	1.36	0.81	0.49
K-band [Burud et al., 1998]	=1	0.965 ± 0.013	0.544 ± 0.025	0.458 ± 0.004
J-band [Burud et al., 1998]	=1	0.885 ± 0.003	0.496 ± 0.005	0.412 ± 0.005
I-band [Burud et al., 1998]	=1	0.680 ± 0.013	0.398 ± 0.002	0.420 ± 0.003
V-band [Burud et al., 1998]	=1	0.587 ± 0.009	0.334 ± 0.004	0.413 ± 0.006
U-band [Burud et al., 1998]	=1	0.590 ± 0.013	0.285 ± 0.007	0.393 ± 0.004

Table 4.2: Table of the fluxes of the images of RXJ0911+0551.

For HE0435-1223, it is immediately noticeable that image C is far brighter than in other frequencies. Since image C is fainter in both [Morgan et al., 2005] and [Fadely and Keeton, 2012b] it is unlikely, but not ruled out to be microlensed, implying that C is suffering from extinction effects. In the RXJ0911+0551 fluxes, image B is much brighter for both the Difmap and *JMFIT* fluxes than in past papers. Additionally, image C is much stronger in both radio fluxes, to the point where the *JMFIT* flux for images A and C are nearly the same. This contrasts with the optical frequencies, where A is at least twice as bright as C. One possible explanation for this could be extinction in the B-C region, with most of the dust near B; another reason could be that image A is brightened due to microlensing. The most probable of the two is extinction, because [Keeton et al., 2003] there is a colour difference between image A and images B and C.

One method for examining substructure in lens systems is to look at the cusp or fold relations. However, these relations do not reveal much about substructure for HE0435-1223 because it is a cross configuration lens. The fold and cusp relations give the most information for fold and cusp configuration lenses respectively. RXJ0911+0551 is a cusp lens system, so if $R_{cusp} > 0$ then there is evidence for substructure in the system. In the radio, for the *JMFIT* fluxes $R_{cusp} = 0.092 \pm 0.018$ and for the Difmap fluxes $R_{cusp} = 0.143$; both are significantly lower than the near-infrared [Keeton et al., 2003] 0.23 ± 0.06. However, the model from [Keeton et al., 2003] predicted that $R_{cusp} = 0.00$ and the radio results are both over 5σ using the *JMFIT* errors from the model. This means that the cusp relation is violated, which indicates the presence of substructure in RXJ0911+0551.

4.2 Modelling

Modelling the lens systems provides another way to find substructure. If the best fit model disagrees with the observations, then that may indicate that dark matter subhalos are interfering. By adding small clumps to the model, it may be possible to determine likely positions and masses of the subhalos. This thesis uses the Igloo lens simulating and fitting program created by Neal Jackson.

Igloo works by taking the input parameters and the galaxy mass distribution model to calculate the deflection angle $\alpha(\theta)$. The source position is then obtained from the lens equation, $\beta = \theta - \alpha(\theta)$. The source position and lens galaxy parameters are then optimised by the AMOEBA downhill-simplex method (Press et al. 1992, Numerical Recipes in C). Igloo computes χ^2 and leaves it up to the user to compute the reduced chi-squared statistic χ^2_{red}. Igloo calculates χ^2 by computing for each component position the offset of the model from the observed position, and then work out $(observed - model)^2/error^2$. This is done in the image plane by finding the roots of the lens equation to get the model postion. The same procedure is done with the expected and observed flux ratios and a χ^2 is calculated, then the individual χ^2 values are added together.

For all the models presented below, the galaxy mass model was the singular isothermal ellipsoid (SIE) and the free parameters were: source position, Einstein radius, lens galaxy ellipticity e, angle ϕ between lens galaxy major axis and the x-axis, shear strength and shear angle. For the HE0435-1223 model, the lens galaxy position was a free parameter because the lens galaxy is not seen in the radio map. The ellipticity is defined as $1-f$ where f is defined in equation 20 and 21 of [Metcalf and Amara, 1994].

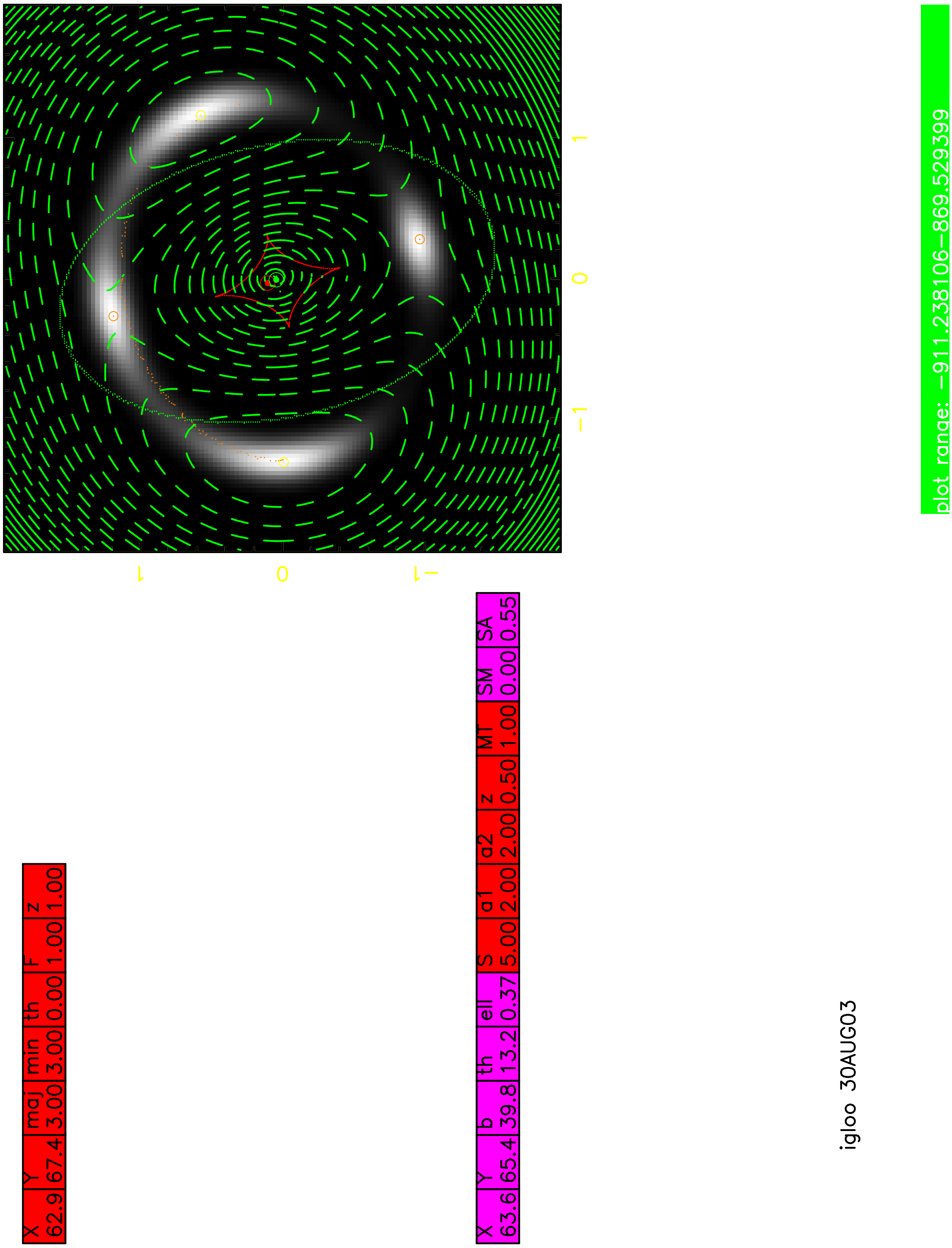

Figure 4.1: This is the Igloo model for HE0435-1223. The green dot denotes the lens galaxy position, the red dot is the source position, the yellow and orange dots are the input image positions, the red line is the caustic curve and the dashed green lines show the lens potential.

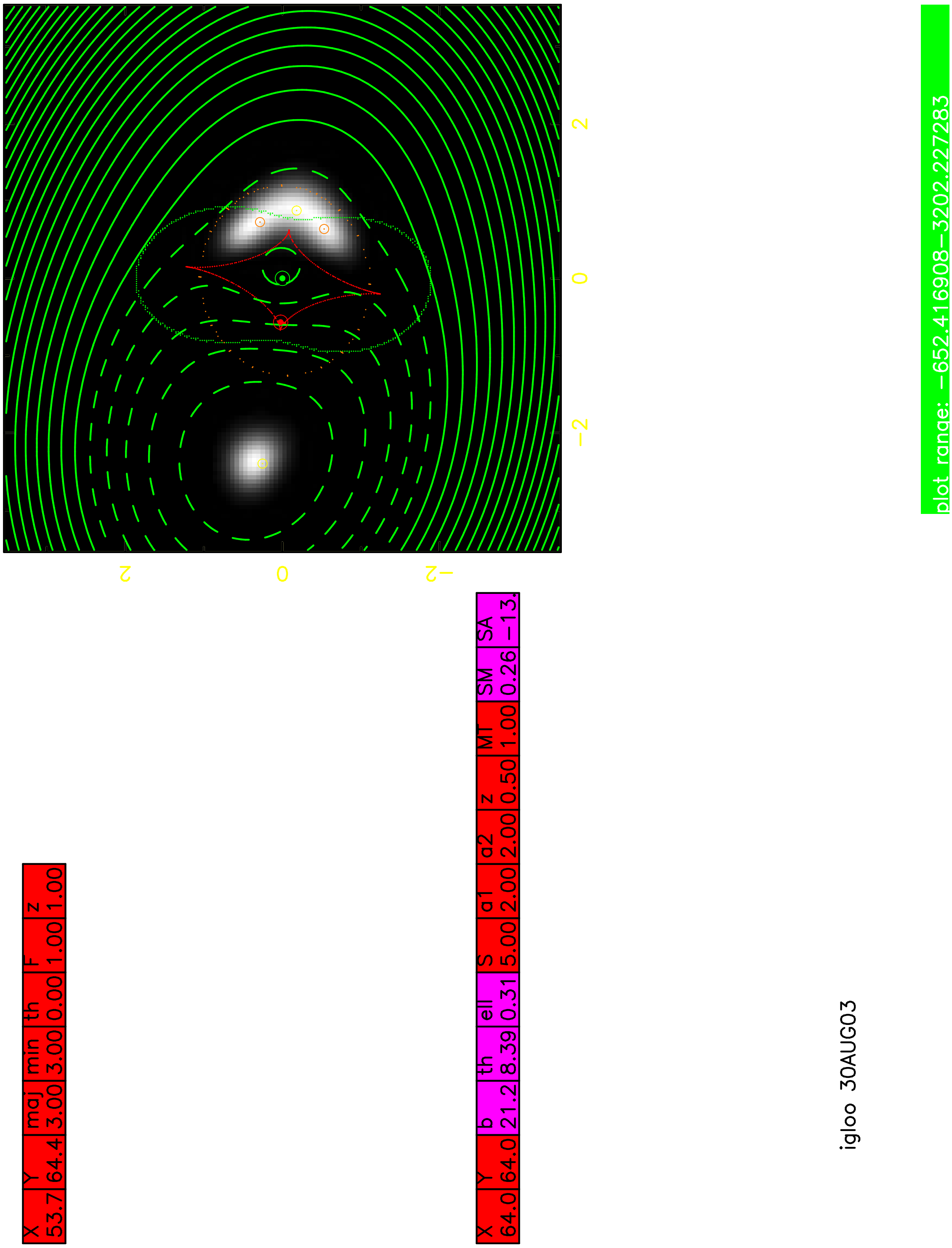

Figure 4.2: This is the Igloo model for RXJ0911+0551

Parameter	Igloo model
x_s (“)	-0.0332
y_s (“)	0.1040
x_l (“)	-0.0106
y_l (“)	0.0438
Einstein radius (“)	1.218
Ellipticity	0.38
ϕ (degrees)	13.3
Shear strength	0.00
Shear angle (degrees)	0.5

Table 4.3: Table of model parameters from Igloo for HE0435-1223. x_l and y_l denote the lensing galaxy position, which allowed to vary because the lensing galaxy is not seen in the radio map, and x_s and y_s denote the position of the source.

Parameter	Igloo model	[Sluse et al., 2012] SIE model
x_s (“)	-0.5681	-
y_s (“)	0.0236	-
Einstein radius (“)	1.175	1.086
Ellipticity	0.32	0.24
ϕ (degrees)	8.4	-72
Shear strength	0.262	0.327
Shear angle (degrees)	-13.5	9.39

Table 4.4: Table of model parameters from Igloo and [Sluse et al., 2012] for RXJ0911+0551. x_s and y_s denote the source position.

χ^2	A	B	C	D
Position (smooth)	0.9	1.1	0.1	1.7
Flux (smooth)	0.3	0.0	0.0	1.3
Position (+clump)	0.0	0.1	0.0	0.1
Flux (+clump)	0.0	0.2	0.5	0.2
Position (L'-band)	1.7	1.0	4.3	1.6
Flux (L'-band)	19.7	0.1	15.7	1.2

Table 4.5: Table of the χ^2 for the fluxes and positions of the images in the various Igloo models of HE0435-1223. The closer χ^2 is to zero, the better the model. The first two row show the goodness-of-fit for a smooth model; this model has $\chi^2 = 4.8$ and has one degree of freedom, so the reduced chi-squared is $\chi^2_{red} = 4.8$. The next two rows show the goodness-of-fit when a clump is introduced near image A; this model has $\chi^2 = 1.2$ but has -3 degrees of freedom. The final two rows demonstrate the goodness-of-fit for the Igloo model for the system using the radio positions and the L'-band fluxes from [Fadely and Keeton, 2012b]. This model has $\chi^2 = 40.1$ and has one degree of freedom, so $\chi^2_{red} = 40.1$.

χ^2	A	B	C	D
Position	69.2	271.1	21.2	5.8
Flux	10.7	0.9	76.9	25.4

Table 4.6: Table of the χ^2 for the fluxes and positions of the images in the Igloo model of RXJ0911+0551. The best-fit model has $\chi^2 = 35.7$ and has three degrees of freedom, so the reduced chi-squared is $\chi^2_{red} = 11.9$.

The smooth SIE model fits the HE0435-1223 system well, reproducing the image positions and especially fluxes better than the smooth model in [Fadely and Keeton, 2012b]. However, the smooth model performed worse on the RXJ0911+0551 system, poorly fitting the positions of A, B and C as well as the flux for C and D. Also, the Igloo model does not match the model produced by [Sluse et al., 2012].

In [Fadely and Keeton, 2012b], there is the claim that there is a subhalo near image A of HE0435-1223. I attempt to confirm whether the claim is true, by adding a small clump next to image A, the results of which can be seen below in Table 4.5 and Figure 4.3. The subhalo is an SIS lens, the additional parameters are the subhalo mass and position.

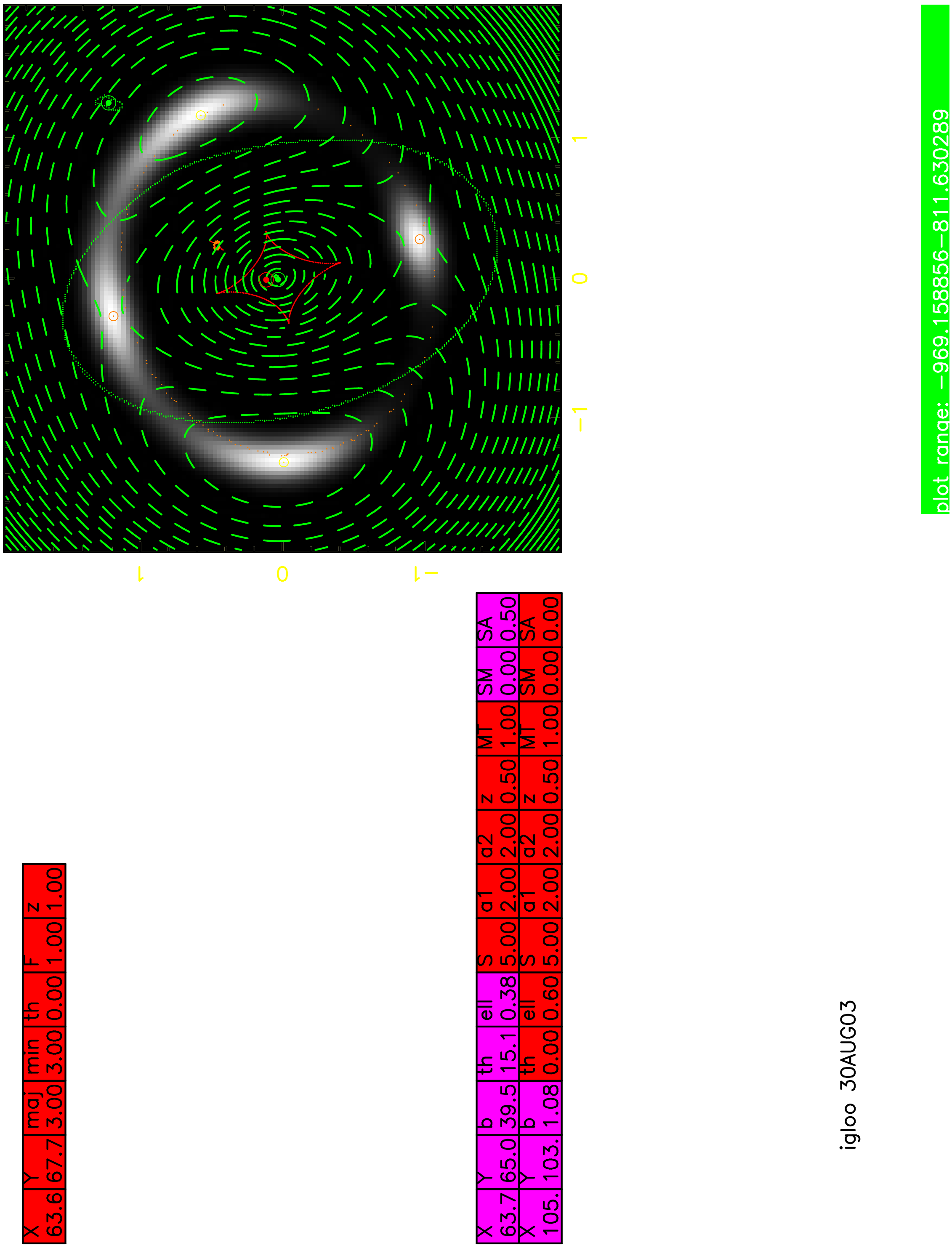

Figure 4.3: This is the Igloo model for HE0435-1223 with an added clump near image A, the green dot in the upper right of the picture.

Parameter	Igloo model
x_s (“)	-0.0105
y_s (“)	0.1141
x_l (“)	-0.0082
y_l (“)	0.0309
Einstein radius (“)	1.208
Ellipticity	0.38
ϕ (degrees)	15.1
Shear strength	0.00
Shear angle (degrees)	0.5
x_c	1.2538
y_c	1.2211
Subhalo Einstein radius (“)	0.033

Table 4.7: Table of model parameters from Igloo for HE0435-1223 with an additional clump near image A. x_l and y_l denote the lensing galaxy position, which allowed to vary because the lensing galaxy is not seen in the radio map. x_c and y_c are the coordinates for the position of the subhalo.

The mass normalisation of the subhalo, expressed as the velocity dispersion σ, can be found by using $b = 4\pi(\sigma/c)^2 D_{ls}/D_s$ where b is the Einstein radius. The velocity dispersion of the clump is $\sigma = 36.4$km/s. Adding a subhalo near image A only improved the model by a small amount, correcting the position and flux of A. Counter-intuitively, it also improved image D but also worsened the fit to image C's flux. The reason why [Fadely and Keeton, 2012b] thought there may be substructure near image A was because their smooth models could not reproduce the observed A/C flux ratio. However, with the radio fluxes this flux anomaly disappears, so smooth models are able to fit HE0435-1223.

Another reason that the model with the radio data is better could be that the radio fluxes have larger errors, so it is easier to fit to them. To test this explanation, I used Igloo to model HE0435-1223 using the [Fadely and Keeton, 2012b] fluxes and the radio positions; the goodness-of-fit of this model is presented in Table 4.5. The best model gives $\chi^2 = 40.1$, worse than before, and it poorly fits the fluxes for both image A and C. This leads to the conclusion that the radio data is not fitted to by a smooth model because of its larger errors. Therefore, the radio data implies that there is no evidence for a subhalo near image A.

Using the models for both lens systems, the image magnifications and the source flux can be computed. The magnifications depend on the model, so the better the fit, the more accurately the original source flux can be obtained. The magnifications of the images and the source flux implied by the images is shown in the table below. The source flux for HE0435-1223 is found to be $8.0 - 9.3\mu$Jy, while the source flux for RXJ0911+0551 is $1.7 - 9.4\mu$Jy. Since the rms noise is of the order of 2μJy for both images, if the source in both systems were not lensed it would be much harder to image it with the same observational parameters. It might have become indistinguishable from the background noise.

	A	B	C	D
Magnification	4.09	-3.14	3.93	-2.08
Flux (μJy)	8.4	8.0	8.1	9.3

Table 4.8: Table of the magnification of the images and the implied source flux in the Igloo model of HE0435-1223.

	A	B	C	D
Magnification	-16.5	20.2	-3.06	1.6
Flux (μJy)	1.7	2.2	8.7	9.4

Table 4.9: Table of the magnifications of the images and the implied source flux in the Igloo model of RXJ0911+0551.

Chapter 5

Conclusion

This work has demonstrated the viability and usefulness of radio imaging radio-quiet lens systems to find evidence of substructure. By obtaining radio fluxes and comparing with optical observations enables the identification of microlensing and dust extinction in images. For HE0435-1223, image C is brighter than in the optical, which may be caused by dust extinction or microlensing in the optical frequencies. This also means that the A/C anomaly in [Fadely and Keeton, 2012b] is not caused by substructure and the radio fluxes can be accurately modelled by a smooth SIE model. Adding the clump reduced the χ^2 from 4.8 to 1.2, however, the degrees of freedom of the model have been reduced from one to -3 so it is over-fitted, therefore, this is not a significant improvement to the model. Therefore, there is no evidence for a clump near image A or for substructure in HE0435-1223. For RXJ0911+0551, image B is brighter and images A and C are the same strength in the radio. This is caused by dust extinction in the B-C region. The cusp relation is violated, for the *JMFIT* fluxes $R_{cusp} = 0.092 \pm 0.018$ and for the Difmap fluxes $R_{cusp} = 0.143$, which indicates that substructure may be present, but the updated cusp violation is not as strong as once thought.

Avenues for future work include performing radio imaging for more radio-quiet lenses. Also if the observations had more observing time, then it may be possible to get more robust flux measurements and also see extended emission to better constrain the models. Improved modelling would also help, by fitting to the uv-plane instead of the image plane, by modelling the source as having finite size [Metcalf and Amara, 2012b] and by providing a full Bayesian test for the evidence of substructure in the lens systems.

Bibliography

T. Anguita, C. Faure, A. Yonehara, J. Wambsganss, J.-P. Kneib, G. Covone, and D. Alloin. Integral field spectroscopy of four lensed quasars: analysis of their neighborhood and evidence for microlensing. A&A, 481:615–627, April 2008. doi: 10.1051/0004-6361:20077306.

N. Bade, J. Siebert, S. Lopez, W. Voges, and D. Reimers. RX J0911.4+0551: A new multiple QSO selected from the ROSAT All-Sky Survey. A&A, 317:L13–L16, January 1997.

K. M. Blundell. Radio-Loud and Radio-Quiet Quasars: One Population, Different Epochs of Observation. In T. A. Rector and D. S. De Young, editors, *Extragalactic Jets: Theory and Observation from Radio to Gamma Ray*, volume 386 of *Astronomical Society of the Pacific Conference Series*, page 467, June 2008.

K. M. Blundell and Z. Kuncic. On the Origin of Radio Core Emission in Radio-quiet Quasars. ApJ, 668:L103–L106, October 2007. doi: 10.1086/522695.

M. Boylan-Kolchin, J. S. Bullock, and M. Kaplinghat. Too big to fail? The puzzling darkness of massive Milky Way subhaloes. MNRAS, 415:L40–L44, July 2011. doi: 10.1111/j.1745-3933.2011.01074.x.

M. Bradač, P. Schneider, M. Lombardi, M. Steinmetz, L. V. E. Koopmans, and J. F. Navarro. The signature of substructure on gravitational lensing in the ΛCDM cosmological model. A&A, 423:797–809, September 2004. doi: 10.1051/0004-6361:20040168.

Y. L. Bukhmastova. Quasars lensed by globular clusters of spiral and elliptical galaxies. *Astronomy Letters*, 33:355–367, June 2007. doi: 10.1134/S1063773707060011.

I. Burud, F. Courbin, C. Lidman, A. O. Jaunsen, J. Hjorth, R. Østensen, M. I. Andersen, J. W. Clasen, O. Wucknitz, G. Meylan, P. Magain, R. Stabell, and S. Refsdal. High-Resolution Optical and Near-Infrared Imaging of the Quadruple Quasar RX J0911.4+0551. ApJ, 501:L5–L10, July 1998. doi: 10.1086/311450.

G. Chartas, X. Dai, S. C. Gallagher, G. P. Garmire, M. W. Bautz, P. L. Schechter, and N. D. Morgan. Chandra Detects a Rapid Flare in the Gravitationally Lensed Mini-Broad Absorption Line QSO RX J0911.4+0551. ApJ, 558:119–126, September 2001. doi: 10.1086/322453.

J. Chen, E. Rozo, N. Dalal, and J. E. Taylor. Astrometric Perturbations in Substructure Lensing. ApJ, 659:52–68, April 2007. doi: 10.1086/512002.

M. Chiba, T. Minezaki, N. Kashikawa, H. Kataza, and K. T. Inoue. Subaru Mid-Infrared Imaging of the Quadruple Lenses PG 1115+080 and B1422+231: Limits on Substructure Lensing. ApJ, 627:53–61, July 2005. doi: 10.1086/430403.

A. B. Congdon, C. R. Keeton, and C. E. Nordgren. Identifying Anomalies in Gravitational Lens Time Delays. ApJ, 709:552–571, February 2010. doi: 10.1088/0004-637X/709/2/552.

N. Dalal and C. S. Kochanek. Direct Detection of Cold Dark Matter Substructure. ApJ, 572:25–33, June 2002. doi: 10.1086/340303.

A. Dekel and J. Silk. The origin of dwarf galaxies, cold dark matter, and biased galaxy formation. ApJ, 303:39–55, April 1986. doi: 10.1086/164050.

E. D'Onghia, V. Springel, L. Hernquist, and D. Keres. Substructure Depletion in the Milky Way Halo by the Disk. ApJ, 709:1138–1147, February 2010. doi: 10.1088/0004-637X/709/2/1138.

E. Eulaers and P. Magain. Time delays for eleven gravitationally lensed quasars revisited. A&A, 536:A44, December 2011. doi: 10.1051/0004-6361/201016101.

R. Fadely and C. R. Keeton. Substructure in the lens HE 0435-1223. MNRAS, 419: 936–951, January 2012a. doi: 10.1111/j.1365-2966.2011.19729.x.

R. Fadely and C. R. Keeton. Substructure in the lens HE 0435-1223. MNRAS, 419: 936–951, January 2012b. doi: 10.1111/j.1365-2966.2011.19729.x.

Y. D. Hezaveh, D. P. Marrone, C. D. Fassnacht, J. S. Spilker, J. D. Vieira, J. E. Aguirre, K. A. Aird, M. Aravena, M. L. N. Ashby, M. Bayliss, B. A. Benson, L. E. Bleem, M. Bothwell, M. Brodwin, J. E. Carlstrom, C. L. Chang, S. C. Chapman, T. M. Crawford, A. T. Crites, C. De Breuck, T. de Haan, M. A. Dobbs, E. B. Fomalont, E. M. George, M. D. Gladders, A. H. Gonzalez, T. R. Greve, N. W. Halverson, F. W. High, G. P. Holder, W. L. Holzapfel, S. Hoover, J. D. Hrubes, K. Husband, T. R. Hunter, R. Keisler, A. T. Lee, E. M. Leitch, M. Lueker, D. Luong-Van, M. Malkan, V. McIntyre, J. J. McMahon, J. Mehl, K. M. Menten, S. S. Meyer, L. M. Mocanu, E. J. Murphy, T. Natoli, S. Padin, T. Plagge, C. L. Reichardt, A. Rest, J. Ruel, J. E. Ruhl, K. Sharon, K. K. Schaffer, L. Shaw, E. Shirokoff, B. Stalder, Z. Staniszewski, A. A. Stark, K. Story, K. Vanderlinde, A. Weiß, N. Welikala, and R. Williamson. ALMA Observations of SPT-discovered, Strongly Lensed, Dusty, Star-forming Galaxies. ApJ, 767:132, April 2013a. doi: 10.1088/0004-637X/767/2/132.

Y. D. Hezaveh, D. P. Marrone, C. D. Fassnacht, J. S. Spilker, J. D. Vieira, J. E. Aguirre, K. A. Aird, M. Aravena, M. L. N. Ashby, M. Bayliss, B. A. Benson, L. E. Bleem, M. Bothwell, M. Brodwin, J. E. Carlstrom, C. L. Chang, S. C. Chapman, T. M. Crawford, A. T. Crites, C. De Breuck, T. de Haan, M. A. Dobbs, E. B. Fomalont, E. M. George, M. D. Gladders, A. H. Gonzalez, T. R. Greve, N. W. Halverson, F. W. High, G. P. Holder, W. L. Holzapfel, S. Hoover, J. D. Hrubes, K. Husband, T. R. Hunter, R. Keisler, A. T. Lee, E. M. Leitch, M. Lueker, D. Luong-Van, M. Malkan, V. McIntyre, J. J. McMahon, J. Mehl, K. M. Menten, S. S. Meyer, L. M. Mocanu, E. J. Murphy, T. Natoli, S. Padin, T. Plagge, C. L. Reichardt, A. Rest, J. Ruel, J. E. Ruhl, K. Sharon, K. K. Schaffer, L. Shaw, E. Shirokoff, B. Stalder, Z. Staniszewski, A. A. Stark, K. Story, K. Vanderlinde,

A. Weiß, N. Welikala, and R. Williamson. ALMA Observations of SPT-discovered, Strongly Lensed, Dusty, Star-forming Galaxies. ApJ, 767:132, April 2013b. doi: 10.1088/0004-637X/767/2/132.

J. Hjorth, I. Burud, A. O. Jaunsen, P. L. Schechter, J.-P. Kneib, M. I. Andersen, H. Korhonen, J. W. Clasen, A. A. Kaas, R. Østensen, J. Pelt, and F. P. Pijpers. The Time Delay of the Quadruple Quasar RX J0911.4+0551. ApJ, 572:L11–L14, June 2002. doi: 10.1086/341603.

J. Hogbom. Aperture synthesis with a non-regular distribution of interferometric baselines. *Astron. Astrophys. Supp.*, 15.

K. T. Inoue and M. Chiba. Three-dimensional Mapping of CDM Substructure at Submillimeter Wavelengths. ApJ, 633:23–28, November 2005. doi: 10.1086/452623.

N. Jackson. The Faintest Radio Source Yet: Expanded Very Large Array Observations of the Gravitational Lens SDSS J1004+4112. ApJ, 739:L28, September 2011. doi: 10.1088/2041-8205/739/1/L28.

C. R. Keeton and L. A. Moustakas. A New Channel for Detecting Dark Matter Substructure in Galaxies: Gravitational Lens Time Delays. ApJ, 699:1720–1731, July 2009. doi: 10.1088/0004-637X/699/2/1720.

C. R. Keeton, B. S. Gaudi, and A. O. Petters. Identifying Lenses with Small-Scale Structure. I. Cusp Lenses. ApJ, 598:138–161, November 2003. doi: 10.1086/378934.

A. Klypin, A. V. Kravtsov, O. Valenzuela, and F. Prada. Where Are the Missing Galactic Satellites? ApJ, 522:82–92, September 1999. doi: 10.1086/307643.

C. S. Kochanek and N. Dalal. Tests for Substructure in Gravitational Lenses. ApJ, 610:69–79, July 2004. doi: 10.1086/421436.

C. S. Kochanek, N. D. Morgan, E. E. Falco, B. A. McLeod, J. N. Winn, J. Dembicky, and B. Ketzeback. The Time Delays of Gravitational Lens HE 0435-1223: An

Early-Type Galaxy with a Rising Rotation Curve. ApJ, 640:47–61, March 2006. doi: 10.1086/499766.

S. Mao and P. Schneider. Evidence for substructure in lens galaxies? MNRAS, 295: 587, April 1998. doi: 10.1046/j.1365-8711.1998.01319.x.

N. Menci, F. Fiore, and A. Lamastra. Galaxy formation in warm dark matter cosmology. MNRAS, 421:2384–2394, April 2012. doi: 10.1111/j.1365-2966.2012. 20470.x.

R. B. Metcalf and A. Amara. . A&A, 284:285–299, 1994.

R. B. Metcalf and A. Amara. Small-scale structures of dark matter and flux anomalies in quasar gravitational lenses. MNRAS, 419:3414–3425, February 2012a. doi: 10.1111/j.1365-2966.2011.19982.x.

R. B. Metcalf and A. Amara. Small-scale structures of dark matter and flux anomalies in quasar gravitational lenses. MNRAS, 419:3414–3425, February 2012b. doi: 10.1111/j.1365-2966.2011.19982.x.

R. B. Metcalf and P. Madau. Compound Gravitational Lensing as a Probe of Dark Matter Substructure within Galaxy Halos. ApJ, 563:9–20, December 2001. doi: 10.1086/323695.

B. Moore, S. Ghigna, F. Governato, G. Lake, T. Quinn, J. Stadel, and P. Tozzi. Dark Matter Substructure within Galactic Halos. ApJ, 524:L19–L22, October 1999. doi: 10.1086/312287.

N. D. Morgan, G. Chartas, M. Malm, M. W. Bautz, I. Burud, J. Hjorth, S. E. Jones, and P. L. Schechter. Chandra X-Ray Observations of the Quadruply Lensed Quasar RX J0911.4+0551. ApJ, 555:1–6, July 2001. doi: 10.1086/321454.

N. D. Morgan, C. S. Kochanek, O. Pevunova, and P. L. Schechter. The Lens Redshift and Galaxy Environment for HE 0435-1223. AJ, 129:2531–2541, June 2005. doi: 10.1086/430145.

J. F. Navarro, C. S. Frenk, and S. D. M. White. A Universal Density Profile from Hierarchical Clustering. ApJ, 490:493–508, December 1997.

D. Ricci, J. Poels, A. Elyiv, F. Finet, P. G. Sprimont, T. Anguita, V. Bozza, P. Browne, M. Burgdorf, S. Calchi Novati, M. Dominik, S. Dreizler, M. Glitrup, F. Grundahl, K. Harpsøe, F. Hessman, T. C. Hinse, A. Hornstrup, M. Hundertmark, U. G. Jørgensen, C. Liebig, G. Maier, L. Mancini, G. Masi, M. Mathiasen, S. Rahvar, G. Scarpetta, J. Skottfelt, C. Snodgrass, J. Southworth, J. Teuber, C. C. Thöne, J. Wambsganß, F. Zimmer, M. Zub, and J. Surdej. Flux and color variations of the quadruply imaged quasar HE 0435-1223. A&A, 528:A42, April 2011. doi: 10.1051/0004-6361/201016188.

P. L. Schechter and J. Wambsganss. Quasar Microlensing at High Magnification and the Role of Dark Matter: Enhanced Fluctuations and Suppressed Saddle Points. ApJ, 580:685–695, December 2002. doi: 10.1086/343856.

P. Scheider, C. Kochanek, and J. Wambsganss. *Gravitational Lensing: Strong, Weak and Micro*. Springer, Berlin, 2006.

D. Sluse, V. Chantry, P. Magain, F. Courbin, and G. Meylan. COSMOGRAIL: the COSmological MOnitoring of GRAvItational Lenses. X. Modeling based on high-precision astrometry of a sample of 25 lensed quasars: consequences for ellipticity, shear, and astrometric anomalies. A&A, 538:A99, February 2012. doi: 10.1051/0004-6361/201015844.

A. Thompson, J. Moran, and G. Swenson. *Interferometry and Synthesis in Radio Astronomy, 2nd Edition*. Wiley, New York, 2001.

C. Tortora, E. Piedipalumbo, and V. F. Cardone. Lens modelling and estimate of H_0 in quadruply lensed systems. MNRAS, 354:343–354, October 2004. doi: 10.1111/j.1365-2966.2004.08160.x.

S. Vegetti and L. V. E. Koopmans. Statistics of mass substructure from strong gravitational lensing: quantifying the mass fraction and mass function. MNRAS, 400:1583–1592, December 2009. doi: 10.1111/j.1365-2966.2009.15559.x.

S. Vegetti, O. Czoske, and L. V. E. Koopmans. Quantifying dwarf satellites through gravitational imaging: the case of SDSSJ120602.09+514229.5. MNRAS, 407:225–231, September 2010. doi: 10.1111/j.1365-2966.2010.16952.x.

S. Vegetti, D. J. Lagattuta, J. P. McKean, M. W. Auger, C. D. Fassnacht, and L. V. E. Koopmans. Gravitational detection of a low-mass dark satellite galaxy at cosmological distance. Nature, 481:341–343, January 2012. doi: 10.1038/nature10669.

C. A. Vera-Ciro, A. Helmi, E. Starkenburg, and M. A. Breddels. Not too big, not too small: the dark haloes of the dwarf spheroidals in the Milky Way. MNRAS, 428:1696–1703, January 2013. doi: 10.1093/mnras/sts148.

M. Vogelsberger, J. Zavala, and A. Loeb. Subhaloes in self-interacting galactic dark matter haloes. MNRAS, 423:3740–3752, July 2012. doi: 10.1111/j.1365-2966.2012.21182.x.

J. L. Wardlow, A. Cooray, F. De Bernardis, A. Amblard, V. Arumugam, H. Aussel, A. J. Baker, M. Béthermin, R. Blundell, J. Bock, A. Boselli, C. Bridge, V. Buat, D. Burgarella, R. S. Bussmann, A. Cabrera-Lavers, J. Calanog, J. M. Carpenter, C. M. Casey, N. Castro-Rodríguez, A. Cava, P. Chanial, E. Chapin, S. C. Chapman, D. L. Clements, A. Conley, P. Cox, C. D. Dowell, S. Dye, S. Eales, D. Farrah, P. Ferrero, A. Franceschini, D. T. Frayer, C. Frazer, H. Fu, R. Gavazzi, J. Glenn, E. A. González Solares, M. Griffin, M. A. Gurwell, A. I. Harris, E. Hatziminaoglou, R. Hopwood, A. Hyde, E. Ibar, R. J. Ivison, S. Kim, G. Lagache, L. Levenson, L. Marchetti, G. Marsden, P. Martinez-Navajas, M. Negrello, R. Neri, H. T. Nguyen, B. O'Halloran, S. J. Oliver, A. Omont, M. J. Page, P. Panuzzo, A. Papageorgiou, C. P. Pearson, I. Pérez-Fournon, M. Pohlen, D. Riechers, D. Rigopoulou, I. G. Roseboom, M. Rowan-Robinson, B. Schulz, D. Scott, N. Scoville, N. Seymour, D. L. Shupe, A. J. Smith, A. Streblyanska, A. Strom, M. Symeonidis, M. Trichas, M. Vaccari, J. D. Vieira, M. Viero, L. Wang, C. K. Xu, L. Yan, and M. Zemcov. HerMES: Candidate Gravitationally Lensed Galaxies and Lensing Statistics at Submillimeter Wavelengths. ApJ, 762:59, January 2013. doi: 10.1088/0004-637X/762/1/59.

L. Wisotzki, P. L. Schechter, H. V. Bradt, J. Heinmüller, and D. Reimers. HE 0435-1223: A wide separation quadruple QSO and gravitational lens. A&A, 395:17–23, November 2002. doi: 10.1051/0004-6361:20021213.

L. Wisotzki, T. Becker, L. Christensen, A. Helms, K. Jahnke, A. Kelz, M. M. Roth, and S. F. Sanchez. Integral-field spectrophotometry of the quadruple QSO HE 0435-1223: Evidence for microlensing. A&A, 408:455–463, September 2003. doi: 10.1051/0004-6361:20031004.

D. D. Xu, S. Mao, A. P. Cooper, L. Gao, C. S. Frenk, R. E. Angulo, and J. Helly. On the effects of line-of-sight structures on lensing flux-ratio anomalies in a ΛCDM universe. MNRAS, 421:2553–2567, April 2012. doi: 10.1111/j.1365-2966.2012.20484.x.

A. Yonehara, M. Umemura, and H. Susa. Quasar Mesolensing — Direct Probe to Substructures around Galaxies. PASJ, 55:1059–1078, December 2003. doi: 10.1093/pasj/55.6.1059.

E. Zackrisson and T. Riehm. Gravitational Lensing as a Probe of Cold Dark Matter Subhalos. *Advances in Astronomy*, 2010:478910, 2010. doi: 10.1155/2010/478910.

E. Zackrisson, T. Riehm, O. Möller, K. Wiik, and P. Nurmi. Strong Lensing by Subhalos in the Dwarf Galaxy Mass Range. I. Image Separations. ApJ, 684:804–810, September 2008. doi: 10.1086/590541.

Appendix

The following is the AIPS script for reducing the data for the first observation of HE0435-1223:

restore 0 dotv -1;docrt 1;indi 1;outdi 1 datain'DATA:EVL-H0435-1.fits outname'H0435';outc

go fitl;wai fitl clro; outdi 1

inna'H0435;incl'UVDATA';refant 28 inext'sn';inv -1;extd inext'cl';inv 2;extd inext'fg';inv -1;extd inext'bp';inv -1;extd cparm 0 0 1 0;go indxr;wai indxr; cparm 0

bif 1; eif 0;bchan 1;echan 2;go uvflg;wai uvflg bchan 63;echan 64;go uvflg;wai uvflg bchan 1;echan 0

object'3C138';band'C';go calrd;wai calrd object";band" calsou'0521+166=3C138';in2na'3C1

calsou'0521+166=3C138' ";in2na'3C138$'_C; in2cl'MODEL'; in2seq1docalib1; gobpass; waibp$

outna inna;avoption'subs';channel 64;go avspc;wai avspc channel 0;avoption";docalib -1;doband -1

inna'H0435';incl'SUB SP';inseq 0

sourc'0521+166=3C138';optyp'calc';go setjy;wai setjy source";optype" calsou'0521+166=3C

1844$'''; gocalib; waicalibsourc'J0437-1844'; calsou'0521+166=3C138'; gogetjy; waigetjysour$

$1cparm100001; gosnsmo; waisnsmocparm0; inv3; snv3; goclcal; waiclcalinv0; snv0$

source'HE0435-1223';docalib 1;inclass";go split;wai split sourc";docalib -1

inna'HE0435-1223';incl'SPLIT' clro outdi 1 cellsi 0.02;imsiz 1024;uvwtfn'na';dotv 0 nbox 2 go imagr;wai imagr